ANNUAL SC...

AD-A245 299

A STUDY OF ...
A RANGE OF ...
INCLUDING ...

Principle Investigator: D...

DTIC
ELECTE
JAN 23 1992

PCS GROUP
Cavendish Laboratory
Department of Physics
Cambridge University
Madingley Road
Cambridge
CB3 OHE
UK

Contract Number: AFOSR 87-0304

Period 1st September 1990 - 31st October 19...

92-01718

92 121 062

This report has been reviewed and is releasable to the National Technical Information Service (NTIS). At NTIS it will be releasable to the general public, including foreign nations.

This technical report has been reviewed and is approved for publication.

CHESTER J. DYMEK, Lt Col, USAF
Chief, Chemistry

RONALD J. LISOWSKI, Lt Col, USAF
Chief Scientist

REPORT DOCUMENTATION PAGE

1a. REPORT SECURITY CLASSIFICATION Unclassified		1b. RESTRICTIVE MARKINGS
2a. SECURITY CLASSIFICATION AUTHORITY		3. DISTRIBUTION / AVAILABILITY OF REPORT Approved for public release; Distribution unlimited.
2b. DECLASSIFICATION / DOWNGRADING SCHEDULE		
4. PERFORMING ORGANIZATION REPORT NUMBER(S)		5. MONITORING ORGANIZATION REPORT NUMBER(S) EOARD TR-92-01
6a. NAME OF PERFORMING ORGANIZATION Cavendish Laboratory University of Cambridge	6b. OFFICE SYMBOL (If applicable)	7a. NAME OF MONITORING ORGANIZATION European Office of Aerospace Research and Development.
6c. ADDRESS (City, State, and ZIP Code) Cavendish Laboratory Madingley Road Cambridge CB3 OHE, UK.		7b. ADDRESS (City, State, and ZIP Code) Box 14 FPO New York 09510-0200
8a. NAME OF FUNDING / SPONSORING ORGANIZATION Aerospace Research & Development	8b. OFFICE SYMBOL (If applicable) LRP	9. PROCUREMENT INSTRUMENT IDENTIFICATION NUMBER AFOSR-87-0384

8c. ADDRESS (City, State, and ZIP Code) P O Box 14 FPO New York 09510-0200	10. SOURCE OF FUNDING NUMBERS			
	PROGRAM ELEMENT NO.	PROJECT NO.	TASK NO	WORK UNIT ACCESSION NO.
	61102F	2301	D1	024

11. TITLE (Include Security Classification)
Studies of rain erosion mechanisms in a range of IR transmitting ceramics including coated samples.

12. PERSONAL AUTHOR(S)
Dr J E Field

13a. TYPE OF REPORT Annual Scientific	13b. TIME COVERED FROM 1.9.90 TO 30.10.91	14. DATE OF REPORT (Year, Month, Day) November 1991	15. PAGE COUNT 79

16. SUPPLEMENTARY NOTATION

17. COSATI CODES			18. SUBJECT TERMS (Continue on reverse if necessary and identify by block number)
FIELD	GROUP	SUB-GROUP	

19. ABSTRACT (Continue on reverse if necessary and identify by block number)
This report contains recent results on ZnS and other IR transparent window systems. Section 1 describes an investigation into the stress corrosion characteristics of ZnS using the double torsion geometry. The results suggest that ZnS is susceptible to moisture enhanced slow crack growth but to a lesser extent than, for instance soda lime glasses. Section 2 discusses the correct experimental procedure for the Brazilian test and then uses this geometry to determine the variation of both ZnS and Ge fracture stress as a function of temperature. The average fracture stress fluctuates (as does the associated error) but remain above the room temperature value within the temperature range -70°C to 600°C. Section 3 contains results from the bursting disc test performed on large (125mm diameter by 5.45mm) ZnS windows rather than small (25mm or 50mm diameter) test pieces. The agreement between the results for the small and large scale samples suggests that the small samples give a good representation of the strength of a full size window and that the surface finish achieved on the small discs can be reproduced in the larger discs. Some results from the Multiple Impact

20. DISTRIBUTION / AVAILABILITY OF ABSTRACT ☐ UNCLASSIFIED/UNLIMITED ☐ SAME AS RPT ☐ DTIC USERS	21. ABSTRACT SECURITY CLASSIFICATION
22a. NAME OF RESPONSIBLE INDIVIDUAL	22b. TELEPHONE (Include Area Code) 22c. OFFICE SYMBOL

DD Form 1473, JUN 86   Previous editions are obsolete.   SECURITY CLASSIFICATION OF THIS PAGE

Jet Apparatus (MIJA) are given in Section 4, decribing the derivation of the threshold velocity for a GeC coated ZnS system. The improvement in threshold velocity over that of the uncoated substrate is marginal. The technique used relies on measuring the maximum velocity at which the specimen was impacted in a given run. Recent developments of the apparatus have reduced the spread in jet velocities and will therefore simplify the procedure for evaluating threshold velocities. The final section details some of the new experimental techniques used in the laboratory for evaluating the mechanical properties of thin films and the thermal upshock resistance of brittle materials. A paper on the sand erosion of CVD diamond films is included as an appendix.

1   INTRODUCTION

This report contains recent results on zinc sulphide and other IR transparent window systems. The first section describes an investigation into the stress corrosion characteristics of zinc sulphide using the double torsion geometry. The results suggest that zinc sulphide is susceptible to moisture enhanced slow crack growth but to a lesser extent than, for instance, soda lime glass.

The second section discusses the correct experimental procedure for the Brazilian test and then uses this geometry to determine the variation of both zinc sulphide and germanium fracture stress as a function of temperature. The average fracture stress fluctuates (as does the associated error) but remains above the room temperature value within the temperature range -70 °C to 600 °C.

The third section contains results from the bursting disc test performed on large (125 mm diameter by 5.45 mm) zinc sulphide windows rather than small (25 mm or 50 mm diameter) test pieces. The agreement between the results for the small and large scale samples suggests that the small samples give a good representation of the strength of a full size window and that the surface finish achieved on the small discs can be reproduced in the larger discs.

Some results from the Multiple Impact Jet Apparatus are given in the fourth section, describing the derivation of the threshold velocity for a germanium carbide coated zinc sulphide system. The improvement in threshold velocity over that of the uncoated substrate is marginal. The technique used relies on measuring the maximum velocity at which the specimen was impacted in a given run. Recent developments of the apparatus have reduced the spread in jet velocities and will therefore simplify the procedure for evaluating threshold velocities.

The next section details some of the new experimental techniques used in the laboratory for evaluating the mechanical properties of thin films and the thermal upshock resistance of brittle materials.

A paper on the sand erosion of CVD diamond films is included as an appendix.

1

2.1 THE STRESS CORROSION OF ZINC SULPHIDE

The stress experienced by a typical zinc sulphide window under standard flight conditions can be calculated and compared to the material's fracture stress. However if the stress levels, while below the critical stress intensity factor, are sufficient to cause sub-critical slow crack growth, delayed failure of the component may occur. The conditions for slow crack growth are discussed in the following section. The extent of this effect for zinc sulphide is then evaluated using the double torsion geometry.

2.2 SLOW CRACK GROWTH IN BRITTLE MATERIALS

Crack propagation in brittle materials initiates when the stress concentrated at the crack tip becomes sufficient to break the chemical bonds there. The critical stress intensity factor (the stress intensity factor (K_I) at which a crack propagates in an inert environment) depends, therefore, on the energy required to break these bonds. In the case of glass, the hydroxyl and hydrogen groups from atmospheric water can attach to the breaking bonds at the crack tip and this process provides a low energy pathway for the cleavage of these bonds. The presence of water in the air, therefore, allows crack propagation to occur at a stress intensity below the critical value. This phenomenon is called stress corrosion.
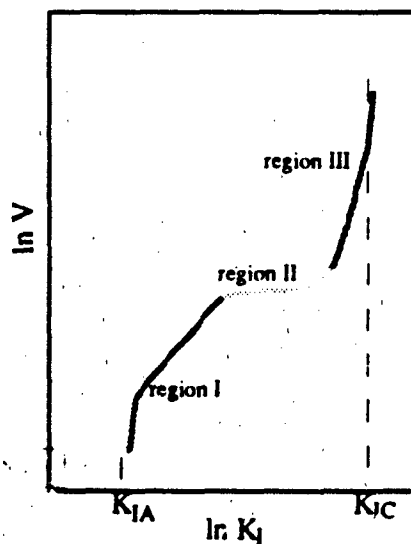

Figure 1
After Pletka and Fuller
(1979).

The graph of crack velocity against stress intensity factor for a specimen in a moist environment has a very distinctive shape and this be seen in Figure 1. K_{IA} is the stress intensity factor above which slow crack propagation occurs in the test atmosphere. K_{IC} is the critical stress intensity factor, the stress intensity factor required to cause a crack to grow in an inert atmosphere. The reasons for this distinctive shape are given below.

2.2.1 Region I

The behaviour in Region I at a constant temperature can be described by the following equation (Lewis and Karunaratne, 1981):-

$$V_c = A \, (\, K_I \,)^n \qquad \qquad (1)$$

where: V_c = crack velocity

K_I = stress intensity factor

A and n are material constants for a given environment

This region is the most crucial for evaluating component lifetimes since it defines the slow crack growth. Once the crack has grown to such an extent that the value of K_I has left the region the component's lifetime can often be measured in seconds. Wiederhorn and Bolz (1970) assessed the effect of increasing temperature on the curve for glass, and showed that, up to temperatures of 90 °C, the line in this region shifts to lower stress intensity factors with no change of gradient (see also Freiman, 1980).

There is a theoretical minimum value of K_I at which there is no crack growth at all (Davidge, 1979), although slow crack growth continues down to such low crack velocities that this minimum is extremely difficult to detect experimentally.

2.2.2 Region II

The distinctive plateau region (Region II) occurs because as the crack accelerates it reaches a regime where the crack velocity is such that the atmospheric water cannot diffuse into the opening crack fast enough to reach the crack tip. This is, therefore, the limiting crack velocity at stress intensities below the critical value (K_{IC}) and is highly dependent on the amount of corroding medium in the atmosphere. The value of K_{IA} is less sensitive to the composition of the atmosphere. In the case of glass for instance, increasing the moisture content of the test environment increases the velocity at which this plateau occurs, while reducing the width of the plateau (Wiederhorn, 1967).

This trend is shown in Figure 2. For tests performed in liquid water the plateau has disappeared completely, since in this case the corrosive medium always has access to the crack tip. This fact was used in a paper by Michalske and Bunker (1987a), which contained a series of experiments with specimens immersed in various organic liquids to determine whether it was the liquid itself, or aqueous impurities carried in the liquid, causing the stress corrosion (if it was the liquid itself then there would be no plateau on the K_I-V curve).
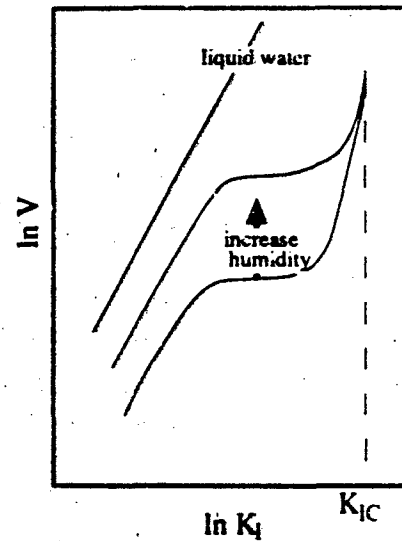

Figure 2
after Wiederhorn (1967).

2.2.3   Region III

When the crack enters Region III it is approaching the point of unstable growth; the stress intensity factor at which the crack will propagate without the moisture induced low energy pathway. As this regime is entered, thermal fluctuations are sufficient to trigger crack growth.

The object of the following series of experiments is to assess the extent to which stress corrosion affects zinc sulphide, and determine whether this factor must be included in calculations for component survivability in the high velocity environment.

4

2.3 THE DOUBLE TORSION GEOMETRY

The experimental geometry selected to determine the variation in velocity with stress intensity factor for zinc sulphide was the double torsion technique (Fuller, 1979; Pletka et al., 1979) depicted in Figure 3 and implemented on an Instron universal testing machine.
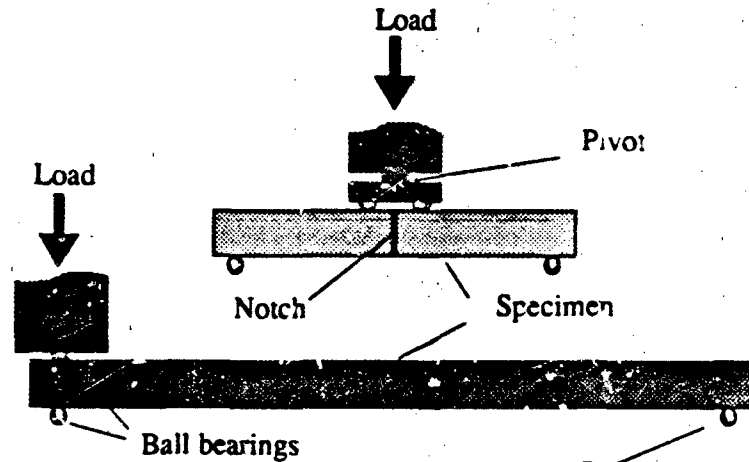
Figure 3
The double torsion apparatus.

If a crack experiences a perpendicular monodirectional tension, the K_I acting at the crack tip depends on the applied stress and the square route of the crack length. Because of this, applying a constant K_I to a moving crack is impractical. The advantage of the double torsion technique is that it is a "constant K_I geometry" (although a torsion is applied to the test piece, Fuller (1979) asserts that crack propagation is of a mode I nature). In other words, for a significant portion of the crack path, the value of K_I is independent of crack length. Thus by applying a constant load to the specimen, the crack can be grown at a constant, easily measurable velocity.

___

The double-torsion geometry was first used by Outwater and Gerry in 1966, and more recently Tait et al. (1987) reviewed the papers on the technique. The experimental design in Figure 3 was taken from a description by Pletka et al. (1979) with modifications suggested by Quinn (1987). The rear ball bearings marked "R" only support the specimen during alignment. Once the anvil is loaded the plate lifts away from them, and the load is applied through the front four points alone. The 3 mm diameter ball bearings are used in preference to rod loading, to more closely approximate point sources. The pivot on the upper anvil ensures an equal distribution of load on the two central ball bearings. In the review paper (Tait et al., 1987) the expression for K_I as found by Williams and Evans (1973) is given as:-

$$K_I = P\ W_m \left(\frac{3}{W\ d^3\ d_n\ (1-v)\ \xi} \right)^{0.5} \qquad (2)$$

Experimental arrangement is shown in Figure 4 where :-

P = applied load
v = Poisson's ratic
d = plate thickness
d_n = web thickness in plate
(for these experiments $d_n = d$ see Section 2.3.4)
W_m = momentum arm
W = plate width
ξ = Correction factor for thick plates
(discussed later in this section)

$$\xi = 1 - 0.6302\ t + 1.20\ t\ e^{-\pi/t} \qquad (3)$$

(Correct to better than 0.1%)

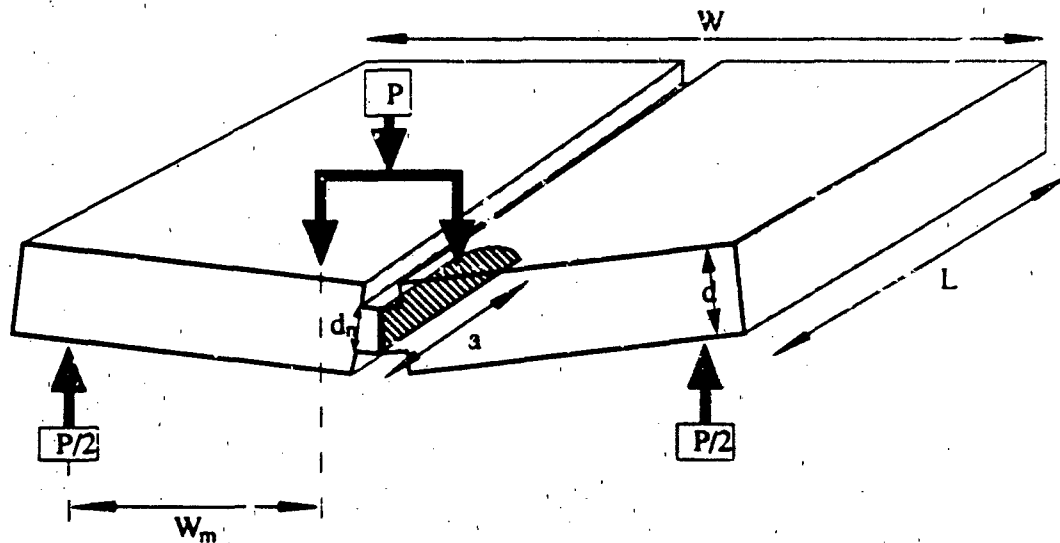where: t = thinness ratio = $2d\ /\ W$

Figure 4

The loading geometry in the double torsion test.

Equation (3) assumes plane-strain at the crack tip which has been found to be approximately true for brittle materials in this experimental set-up (Tait et al., 1987).

The three most common procedures that can be used with the double-torsion apparatus are described by Lewis and Karunaratne (1981) and are discussed below :-

6

5.3.1 The Load Relaxation Procedure

An analysis by Williams and Evans (1973) revealed a linear relationship between compliance and crack length. They then showed that at constant displacement, the crack velocity could be directly related to the instantaneous load (P) and load relaxation rate (dP/ dt) by :-

$$V_c \sim - \frac{(P_{i,f})(a_{i,f})}{P^2} \frac{dP}{dt} \qquad \{4\}$$

where:

P_i = initial load

P_f = final load

a_i = initial crack length

a_f = final crack length

Therefore once crack motion has initiated, the cross-head displacement can be fixed so that as the crack propagates, the compliance increases, the load relaxes, and thus the crack decelerates. Data for a range of crack velocities can therefore be obtained from a single trace. Figure 5 shows a typical load relaxation curve.
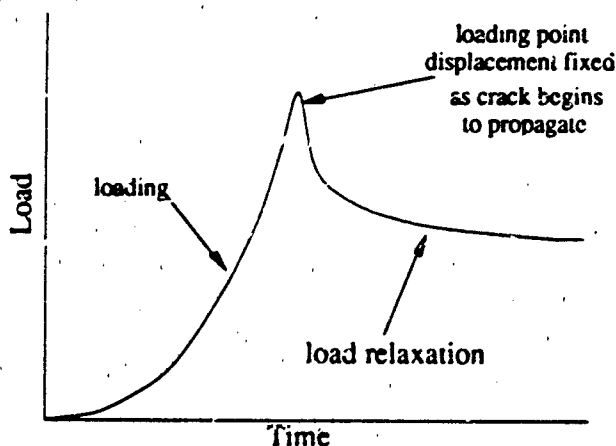

Figure 5
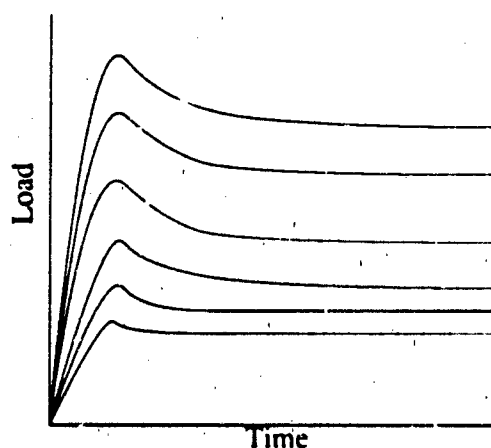A typical load relaxation curve.

Figure 6
Load relaxation calibration graphs.

The load relaxation, however, is not due entirely to the extension of the crack because the fixtures of the test machine will also relax under the applied load. A series of curves must therefore be obtained characterising the background relaxation as a function of load and time (Figure 6). In the present tests this was achieved by loading a blank specimen (with neither notch nor scratch) to progressively higher loads, holding the cross-heads fixed at

7

each load and tracing the load decay. This relaxation must be deducted from the crack relaxation to obtain valid velocity data. It is here that the inherent inaccuracy of the load relaxation experiment becomes apparent, that is that the analysis relies on subtracting one gradient from another. As the velocity decreases, the graph becomes flatter and approaches the gradient of the background graph that must be subtracted from it, increasing the percentage error. Clearly the usefulness of this technique is restricted to measurements at the upper end of the velocity scale.

2.3.2   The Constant Displacement Rate Procedure

This technique relies on the discovery by Evans (1972) that for a constant displacement rate, the trace of load against time flattens out and the height of this plateau is related to the crack velocity. This method only allows one value to be obtained per run. which limits its usefulness in experiments on expensive materials such as zinc sulphide. As with the previous procedure, this technique is inaccurate at low velocities.

2.3.3   The Constant Load Procedure

For low crack velocities, the crack extension over a certain period must be measured directly. The Instron testing machine used had no direct load control, so the cross-head displacement had to be held constant and the fixtures made as stiff as possible to prevent load relaxation. The sample was loaded to the required value, then left for a predetermined time. The load was released and the increase in crack length determined with a travelling microscope. Any relaxation of the load in that time was included as an error in the load value on the graph. In the present series of experiments this error was minimal compared to the inherent inaccuracy of the Instron chart recorder.

In the following experiments both load relaxation and constant load tests were performed. The value of K_I being calculated from Equation (3), and the corresponding velocity determined either by direct measurement, or by using Equation (5).

2.3.4   Experimental Considerations

While the double   sion geometry is easy to perform and the data analysis is straightforward due to its "constant K_I" nature, there are some precautions that need to

be taken to ensure the validity of the results. These precautions and some of the underlying assumptions of the theory are summarised in the review paper by Tait et al. (1987).

The paper lists the wide range of different dimensions suggested for the specimen and, based on the quality of results obtained in each case, goes on to recommend the proportions 3W to W to (1/8-1/12)W. The specimen dimensions used in this study (60 mm by 20 mm by 3 mm i.e. 3W to W to 1/6.7 W) were slightly thicker than these optimum dimensions, but not by enough to invalidate the data, especially when the thickness correction is included. In fact these proportions were used by Tait and Garrett themselves in 1985.

In its original form, the configuration relied on grooves on either or both of the faces of the plate to guide the crack along a central path. Fuller in 1979, in a summary of associated theories, suggested that these grooves could influence the crack growth by introducing stress concentrations into the material. He therefore advocates eliminating the grooves and relying on accurate alignment of the experimental fixtures to ensure the required crack path. Quinn (1987), among others, used this technique successfully, and it was his geometry and sample preparation that was adopted for the present series of tests.
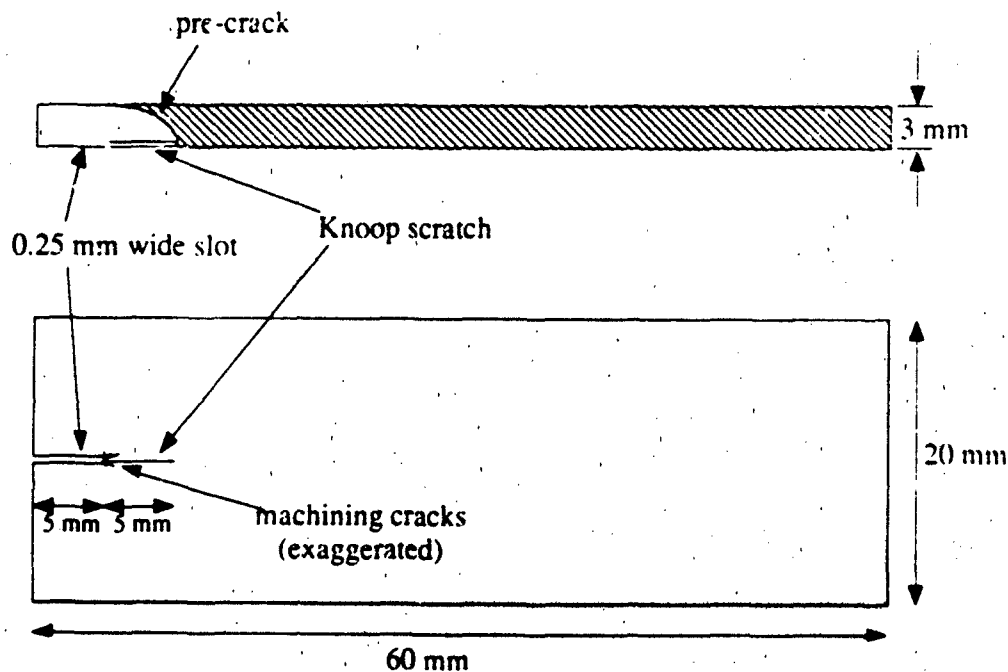

Figure 7
Specimen preparation.

The ungrooved sample is first notched with a 0.25 mm wide diamond saw to a depth of 5 mm as in Figure 7. Great care is taken in the alignment of the notch, and the cutting is performed slowly to avoid machining cracks. Since it is impossible to eliminate these cracks altogether, a 5 mm scratch is carved into the tensile face of the specimen by dragging a Knoop indenter across the surface under a 1 kg load. The pre-crack will then follow the path of the scratch rather than any of the machining cracks. The sample is loaded slowly in the testing rig until the pre-crack pops in. If the pre-crack follows the path of the scratch, and the test fixtures are very carefully aligned with the sample, the test will be successful and the specimen will crack neatly into two halves.

The third important consideration is the thickness correction factor included in Equation (4). The need for this factor arises from the modification of the theoretical stresses caused by the interpenetration of the two arms of the plate. This is made clearer in Figure 8.
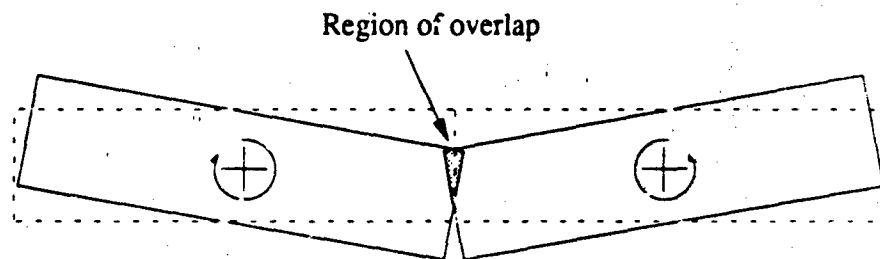

Figure 8
The reason for the inclusion of a thickness correction factor.

As the two arms rotate, the marked regions attempt to overlap. The contact stresses, caused by the two faces pushing against each other, will increase with specimen thickness causing a thickness dependent correction to the stress intensity factor (Fuller, 1979). In the present study $t = 2d / W = 0.3$ and Equation (4) gives a value of $\xi =0.811$. This value must be included in the calculation of K_I.

The fourth consideration is the portion of the crack length for which the assumption of constant K_I is valid, and not distorted by end effects. Again there is some discrepancy over the quoted ranges of acceptable crack lengths. The range of validity is usually assessed by fast loading specimens with pre-cracks of various lengths, and plotting the variation of K_{IC} with the crack length. The discrepancy arises from the different specimen sizes and shapes used by the various authors. The paper by Tait et al. (1987) compiles data from a large number of sources to give validity ranges dependent on the ratio of L to W (i.e the ratio of specimen length to width). For the present tests $L / W = 3$ and for

these proportions the constant K_I assumption is valid for crack lengths from **0.05 L** to **0.85 L**. Data was therefore discarded outside this range.

Finally, the theory assumes that the crack front profile in the test is a straight line, perpendicular to the surfaces. In fact this is not the case, the crack front is curved and the crack length is greater on the tension side than on the compression side (as shown in Figure 4). Since the crack propagates locally perpendicular to the crack front, the crack velocity is not uniform through the depth, although within the valid region the crack propagates without change of shape. There have been several attempts to allow for this potential source of error (see Tait et al., 1987) but none of these have been fully satisfactory, and appear no more valid than taking the velocity of the intercept with the tensile face as the measured crack velocity (Michalske et al., 1981).

As long as these considerations are adhered to, the double torsion technique should produce valid data for a range of crack velocities, in a range of environments.

2.4   RESULTS FOR SODA-LIME GLASS

Because of the high cost and limited availability of zinc sulphide, the experiment was performed initially with soda-lime glass, so that the results could be compared with earlier data. Figure 9 shows the K_I against velocity diagram obtained from both load relaxation and constant load experiments. The results from different runs of the same version of the experiment are in close agreement, as are the results from the two different applications of the geometry (load relaxation and constant load) to within the inherent accuracy of the Instron chart recorder. The relative humidity on the day of the tests was 56%.
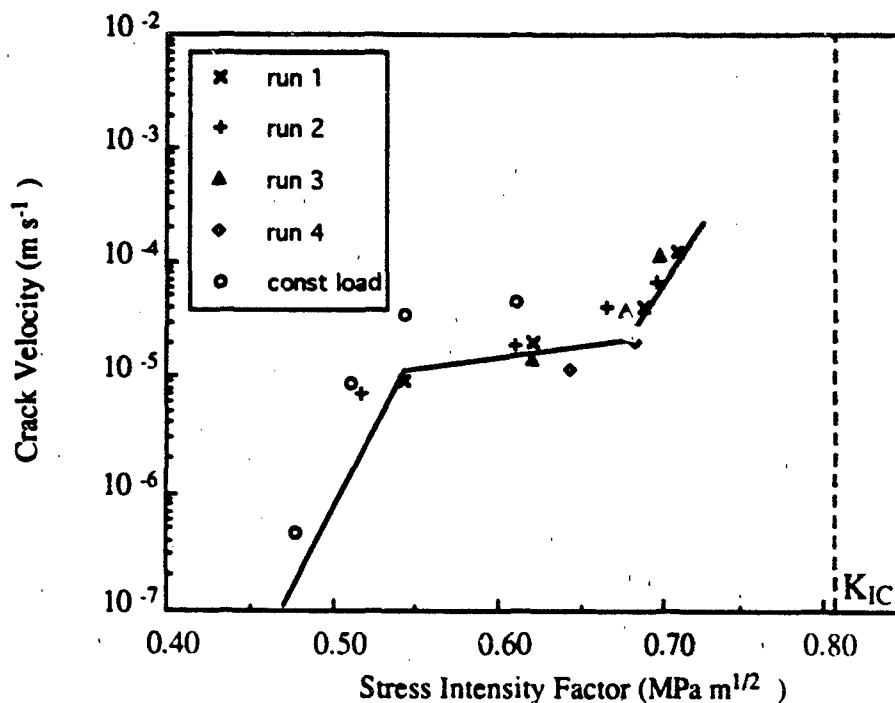
Figure 9
The stress corrosion curve for soda-lime glass.

A value of K_{IC} was obtained by conducting the experiment with the sample immersed in oil to prevent any moisture induced slow crack growth. The value of 0.81 ± 0.1 MPa m$^{1/2}$ agrees well with the slow crack growth data in Figure 9.

The reproducibility of these results, and the close similarity with those obtained by Wiederhorn (1967), suggested that the test was accurate enough to use on the zinc sulphide specimens. Glass, however, is very susceptible to stress corrosion, and has no grain boundaries, second phase particles or other microstructure to interact with the crack. it is an ideal material for stress corrosion tests. Materials with more complex structures often give results which are less clear.

12

2.5 STRESS CORROSION OF GLASSES IN THE LITERATURE

There has been considerable work done on the environmental dependence of the strength of glass, beginning with the discovery of the loading rate dependent variation of glass strength in 1899 by Grenet. Charles and Hillig (1961), Wiederhorn (1967, 1970, 1989), Freiman et al. (1985) and others have since put the theories of stress corrosion on a more quantitative basis.

Michalske and Bunker recently summarised some of their work on glass (1987a) in an excellent overview of the stress corrosion of glass (1987b). It explains the different corrosion characteristics of various environments in terms of the physical size of the active molecules in that environment, and the resultant ease with which they can reach the bonds at the crack tip. It also proposes the low energy pathway for bond rupture in the presence of water, which allows slow crack growth below the critical stress intensity factor, and gives evidence that the bonds strained under the action of the applied stress, react more easily than unstrained bonds. It is the combination of the two factors, stress and environment, that is required for slow crack growth through the stress corrosion mechanism.

The effect of stress corrosion in toughened glasses was examined by Hagan, Swain and Field (1978). They showed that if data on the stress state in the glass are available, a value for the n parameter can be obtained which compares well with estimates from normal glass.

It is interesting to note, however, that the presence of water is not always detrimental to the strength of some glasses. The work of Ito and Tomozawa (1982), and Hirao and Tomozawa (1987a, 1987b) investigated the increase in strength of abraded high silica glass rods immersed in water. This was found to be due to crack blunting, caused by dissolution and reprecipitation of the glass into and out of the water. In Hirao and Tomozawa (1987a) it was found that this crack blunting increases the n-value (from Equation (2)) since a sharp crack is required for slow crack growth, and this has first to be initiated from the blunt crack. Simmons and Freiman (1981) suggested that the region I crack velocity is determined by the opposing mechanisms of corrosive crack tip blunting and stress-corrosive crack tip sharpening.

2.6   RESULTS FOR ZINC SULPHIDE

The K_I against velocity diagrams obtained using the load relaxation technique for two different runs on zinc sulphide in air of relative humidity 52% are presented in Figure 10 and Figure 11.
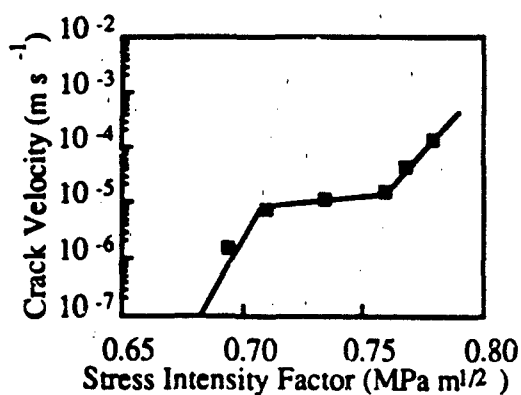
Figure 10

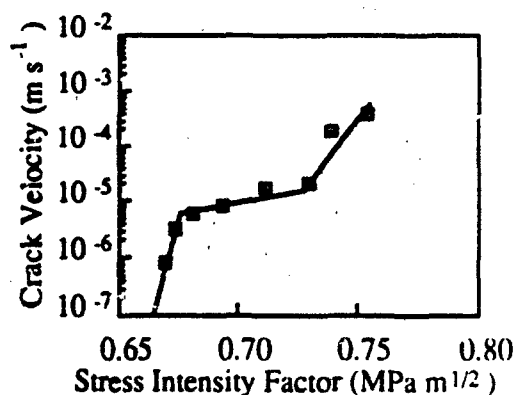The stress corrosion curve for zinc sulphide in air.

Figure 11

The stress corrosion curve for zinc sulphide in air.

It should be noted that the K_I scale for the zinc sulphide data is expanded when compared with the glass results in Figure 9. The shapes of the two traces are identical but there is a slight shift in the stress intensity factor, which indicates the scale of the error in the results introduced by the Instron chart recorder. These graphs show that zinc sulphide is susceptible to stress corrosion, but less so than glass, although the plateau velocities are both roughly 10^{-5} m s^{-1}. Since the height of this plateau is determined by the ease of access of the water molecules to the crack tip then this result would be expected if the crack width was similar in the two materials. The crack width depends on the parameter $K_I (1 + v) / E$ (Lawn and Wilshaw, 1975). This parameter has a value for glass of 1.3×10^5 m$^{1/2}$ and for zinc sulphide of 0.9×10^5 m$^{1/2}$, suggesting that the crack dimensions are indeed similar.

In order to test the effect that an increase in humidity would have on the crack velocity, the test was repeated with the sample completely immersed in water to give a "worst case" situation. The results for this experiment are given in Figure 12 and Figure 13. Again the shapes of the two tests are the same and there is a similar error in the K_I reading. The plateau in the data is an artifact caused by the chart recorder pen's inability to respond fast enough to follow the rapid decrease in load at high crack velocities (Section 2.2.2 explained that for complete immersion in the corrosive medium there would be no plateau).
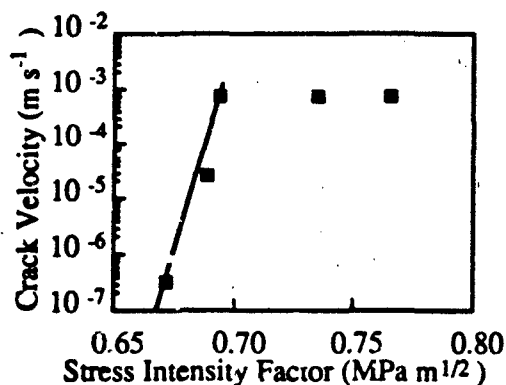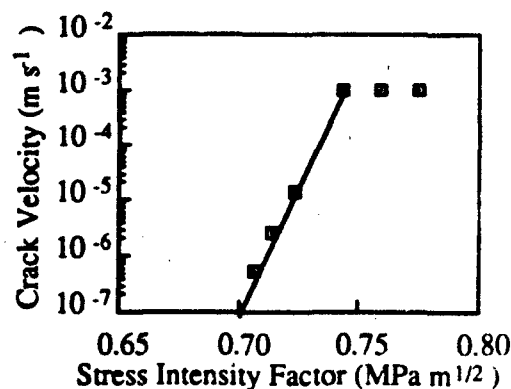
Figure 12

The stress corrosion curve for zinc sulphide in water.

Figure 13

The stress corrosion curve for zinc sulphide in water.

The K_I value at which the crack velocity sharply increases should coincide with the critical stress intensity factor (K_{IC}) of the material. This constant varies slightly with the test used to assess it, and with the grain size of the material (Townsend and Field, 1990). An independent measurement of K_{IC}, obtained by the Vickers indentation technique, described by Lawn and Fuller (1975), gave a value of 0.61 MPa $m^{1/2}$. This technique was chosen because it could be performed on one of the fragments from the double torsion test, thus saving on the number of specimens used. This result is slightly lower than previous measurements (Savage, 1985) and these external results agree more closely to the data in the double torsion graphs (Figures 10 to 13).

Constant load tests were also attempted for zinc sulphide, but no slow crack growth was seen. It is possible that this is due to crack pinning at grain boundaries, an example of an interaction with the zinc sulphide microstructure. A similar microstructural interaction was observed by Quinn (1987) in several materials.

High temperature load relaxation tests on zinc sulphide were also unsuccessful because of temperature induced expansion of the test fixtures. The load variation caused by this expansion swamped the relaxation due to the propagating crack, and wasn't reproducible: it therefore could not be calibrated out of the trace.

If the data from Figure 12 are plotted on a log-log scale, a value of 215 can be obtained for n in Equation (2). Similarly, the data from Figure 13 give a value of 181. The discrepancy between the two results is not unexpected considering the inherent errors in the technique, and as will be seen in the next section, other techniques of measuring this parameter produce far larger errors. For comparison, the n parameter has a value of 16 for soda-lime glass and 31 for alumina (Wahl and Tustison, 1990). In other words zinc sulphide is far less susceptible to stress corrosion than either of these materials.

15

2.7 STRESS CORROSION OF ZINC SULPHIDE IN THE LITERATURE

Two references to the stress corrosion characteristics of zinc sulphide were found. The first (Wahl and Tustison, 1990) predicted no dependence of biaxial flexure strength on stressing rate and no difference was found between the strength at liquid nitrogen temperatures (77K) and room temperatures (therefore n = infinity). In direct contrast to this, in a private communication from the Kaman sciences Corporation in Colorado Springs, a similar experiment was described (using the four point bend test at various loading rates) with the samples immersed in distilled water in which a value of 76 was obtained for n, suggesting a small, but real, susceptibility to moisture enhanced flaw growth. The apparent discrepancy emerges from the inaccuracy in the fracture stress measurements. The error bars displayed on the data by Wahl and Tustison are such that values of n can be obtained from the data which agree with the value quoted by the Kaman Sciences Corporation. This emphasizes the importance of repeating tests on brittle materials that rely on an unknown flaw distribution, so as to reduce the error as much as possible. The double torsion test, using it does a single macroscopic crack of known dimensions, is not susceptible to this inher error.

It is worth mentioning at this point that results for the similar IR candidate material zinc selenide are more numerous. Evans and Johnson (1975) give values of n = 45-95 for tests performed in both air and water and a value of $K_{IC} = 0.9 \ MNm^{-3/2}$. They also encountered intermittent crack propagation, where the crack slowed, then accelerated, suggesting an interaction with the zinc selenide microstructure. It is a similar interaction in the case of zinc sulphide which, it is postulated, caused the failure of the constant load experiment. A study of the extensive effect that microstructure has on zinc selenide can be found in a paper by Freiman et al. (1975).

2.8   CONCLUSIONS

The double torsion test has provided reliable and reproducible results, but only because several precautions were taken in the experimental design, and great care was taken with the preparation and alignment of the specimens.

The experiments in this section have shown that stress corrosion is a factor that must be considered when designing a zinc sulphide infrared window. Fortunately the effect is not as severe as it is for glass. It is worth pointing out that aerodynamic pressures produce tension on the internal face of the window. The humidity behind the window is often artificially reduced to prevent frosting on the inside of the window (Driggers and Tidwell, 1989) and this will also reduce the effects of stress corrosion.

3.1 THE FRACTURE STRESS OF ZINC SULPHIDE AS A FUNCTION OF TEMPERATURE

Aerodynamic heating at stagnation points on aircraft surfaces during high velocity flight can cause temperatures of up to 500 °C at Mach 3. Away from this point of maximum aerodynamic heating the temperature can drop as low as the average air temperature of - 56.5 °C at a height of 11 km.

Because of the wide range of operating temperatures it is necessary to evaluate the fracture stress of zinc sulphide as a function of temperature, to determine whether or not the room temperature design strengths hold true for the whole temperature range that the window is likely to encounter. Unfortunately the bursting disc test described in Appendix 1 is unsuitable for this application because of the temperature sensitivity of the neoprene diaphragm and pressurizing oil, so a second strength test had to be found for this series of experiments. The geometry selected was the so called "Brazilian test".

3.2 THE BRAZILIAN TEST

The Brazilian test shown schematically in Figure 14, first used by Carneiro and Barcellos in 1953, involves the compression of a disc across its diameter to induce failure in tension at the centre of the disc. The advantages this geometry has over other candidate techniques and the precautions that must be taken to ensure the validity of the data obtained will be discussed in the next section.

Figure 14
The Brazilian test.

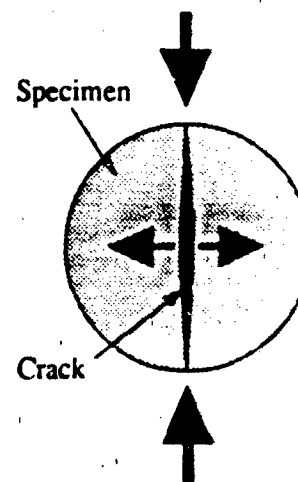## 3.2.1 Experimental Description

The Brazilian test is an "indirect tensile" technique, in other words although the failure is tensile, the tension results from a perpendicular compression. A compressive load is easier to apply to a sample than a tensile one, since the latter requires great care in the design of the grips to prevent stress concentrations and subsequent failure at the loading
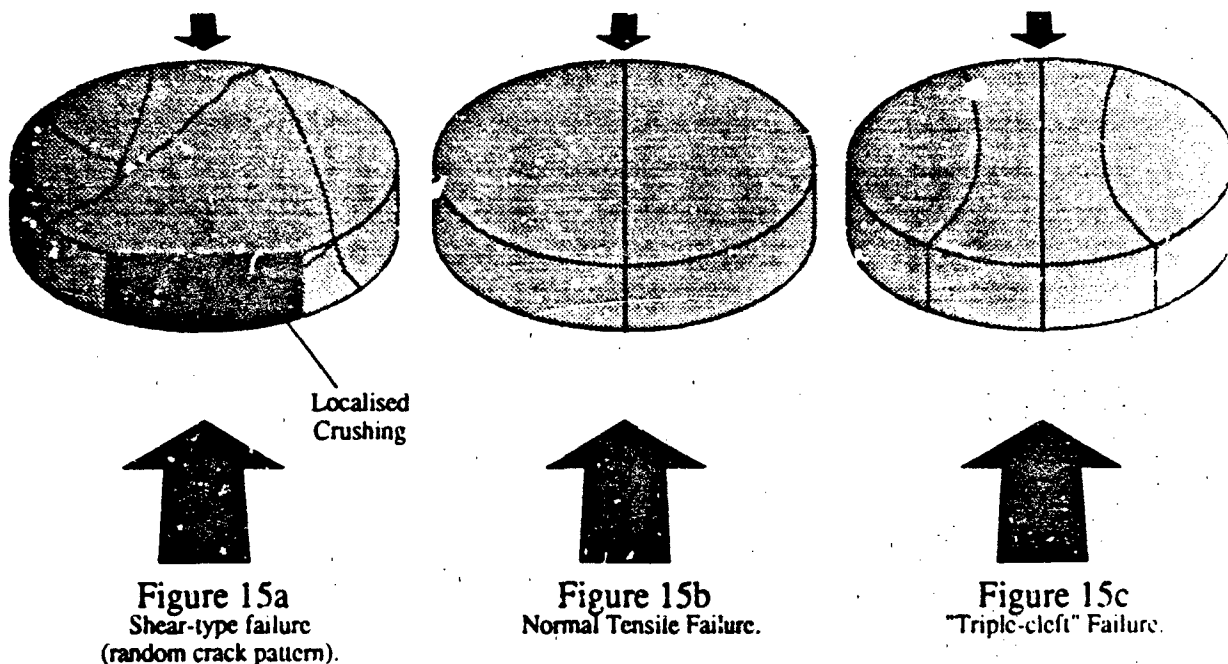
points. The simplicity of the anvils allows the test to be more readily miniaturised and the whole apparatus can easily be enclosed within an environmental chamber and oven. A reduction in sample size is also an advantage because of the high cost of the test materials. Bend tests, a possible alternative, often fail from the edges of the specimen and maximise the stress at the surface, thus accentuating any surface condition dependence that the strength of the material may have.

The Brazilian test was described in a paper by Hondros (1959), in which he includes the theoretical stresses along the axes of the disc perpendicular and parallel to the line of compression. These stress maps show that the tension is greatest in the central half of the disc perpendicular to the compression axis and failure at this point will lead to a crack down the middle of the specimen along the loading axis. Referring to the stress maps produces the fracture stress of the material.

Fairhurst (1964) suggested that the fracture stress assessed by this theory can give misleading results. The values obtained in the test were below those determined by other experimental techniques by an amount which depended on the ratio between the material's uniaxial compressive and tensile strengths, on the size of the loaded region and on tangential stresses along the loaded rim. The ramifications of this discovery will be discussed later.

In an analysis of the Brazilian test by Rudnick et al. in 1963 they summarised the failure modes observed as follows:-

1. Compression and shear failure -   Local crushing at anvils, irregular
                                       fracture pattern.(Figure 15a)
2. Normal tension failure -   Cracks into two halves.(Figure 15b)
3. Triple-cleft failure -   Cracks into four pieces.(Figure 15c)

19

Localised
Crushing

Figure 15a
Shear-type failure
(random crack pattern).

Figure 15b
Normal Tensile Failure.

Figure 15c
"Triple-cleft" Failure.

The first failure geometry gives no useful data about the fracture stress, but both the second and third fail initially along the central axis and provide accurate values for fracture stress (the triple-cleft failure occurs subsequent to the central cracking as the separated halves of the sample briefly support the full load). In the following series of experiments all three failure modes were observed but the first was eliminated by careful specimen alignment.

In the Rudnick paper it is suggested that padding is used at the loading anvil for the following reasons :-

1. To smooth over any asperities in the loading surface to produce a uniform load.
2. To reduce the magnitude of the maximum compressive and shear stresses at the anvils. (Thus inhibiting the shear failure mode)
3. To cause the stress across the loading axis to depart from uniform tension at the anvils. (Thus promoting central failure in the specimen)
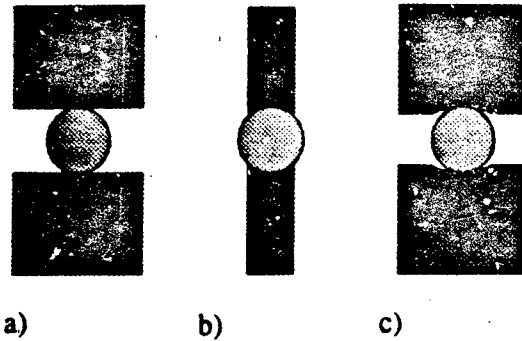
a)   b)   c)

Figure 16

Brazilan test anvil geometries.

Until Awaji and Sato in 1979 the Brazilian test discs were compressed between plane anvils as shown in Figure 16a (Hondros 1959, Fairhurst 1964, Vardar and Finnie 1975). Awaji and Sato's refinement to the technique was to use circular anvils of a radius greater than that of the specimen (Figure 16c), to spread the loading area and minimise the crushing at the contact points. Rabie and Meguid (1986) used a similar geometry but with the radii of the specimen and anvils identical (Figure 16b). This had the disadvantage that there is an anvil corner in contact with the sample which could act as a stress concentrator as the specimen deforms. It was therefore the geometry shown in Figure 16c that was used in the following experiments. The Hertzian contact formulae for this geometry as quoted in the paper by Awaji and Sato are given below.

The width of the region of contact between the anvil and the specimen, $2b$, can be calculated from :-

$$\left(\frac{b}{r}\right)^2 = 4 \frac{r}{(r-R)} \sigma_P \alpha \tag{5}$$

where:

$$\alpha = \frac{1-v_1^2}{E_1} + \frac{1-v_2^2}{E_2} \tag{6}$$

and:
  r = anvil radius
  R = specimen radius
  E = Young's modulus, for anvil (1) and specimen (2)
  v = Poisson's ratio, for anvil (1) and specimen (2)
  σ_P = uniformly distributed stress across loading axis in disc

$$\sigma_P = \frac{P}{\Pi R t}$$

where: P = load
      t = thickness of disc

This value of **b** can then be used with σ_P to give σ_H, the maximum tensile stress at the centre of the disc :-

$$\sigma_H = \left(1 - \left(\frac{b}{R}\right)^2\right)\sigma_P \qquad (7)$$

or more accurately:

$$\sigma_H = \left(1 - 1.15\left(\frac{b}{R}\right)^2 + 0.22\left(\frac{b}{R}\right)^3\right)\sigma_P \qquad (8)$$

These theoretical stresses were compared with photoelastic measurements obtained in a similar geometry to that used in the present study, by Hand (1987).

After this series of experiments was initiated, Darvell (1990) published a review of indirect tensile techniques in which some doubt was raised over the validity of Brazilian test data. One of his concerns was the large variation in the literature in the recommended values for the ratio of the width of the loaded region to the diameter of the specimen, needed to give an accurate fracture stress. This ratio must be sufficiently large to prevent failure due to high contact stresses. He also suggests that the thickness of disc be less than a sixth of the diameter (Wijk, 1978) to prevent higher edge stress at the generators than at the centre of the disc, but observes that this is rarely adhered to : this study the disc specimens were 3 mm thick and 15 mm in diameter). He goes on to state four criteria that must be fulfilled for the theoretical treatment to be valid :-

1. Material is homogeneous.
2. Hooke's law is obeyed up to the point of failure.
3. Geometry is plane stress.
4. Material is isotropic.

The first two assumptions are approximately correct for zinc sulphide but the specimen geometry is not truly a plane stress geometry and the material is crystalline and therefore not isotropic.

The paper also draws attention to the large range of failure modes observed in the test. He suggests the possibility that even a single diametral crack may originate from the anvils rather than the centre of the disc and indeed cited several papers where this appeared to be the case.

Darvell's conclusions do not in any way invalidate the data of the present study, although they are very critical of the Brazilian test as an isolated technique for determination of

material fracture stress. He states that while the true tensile strength is difficult to obtain from this geometry, the test is entirely legitimate for comparative tests of similar materials. Furthermore because of the biaxial nature of the test (one axis in tension, one in compression) the measured fracture stress is less than that obtained by a uniaxial test or the axially symmetric burst test (Fairhurst, 1964; Shaw, 1984). The Brazilian test results at room temperature are, therefore, compared with data on an identical batch of material from the burst test (Matthewson and Field, 1980). For a similar series of tests Hand (1987) found that the fracture stresses measured by the Brazilian test were consistently 65 ± 3% of the burst test results.

In the present study a specimen is tested at a range of temperatures to give comparative data with a baseline value obtained from a second direct tensile test (the bursting disc test described in Appendix 1). It must, however, be ensured that the initial failure is essentially tensile in nature, and is the same throughout the tests. It is felt that despite the reservations expressed above, use of the Brazilian test for the intended application is entirely justified.

3.3 EQUIPMENT

3.3.1 Introduction

The actual rig used to perform the test is shown in cut-away in Figure 17. The lid is removable to allow access to the chamber and, when in operation, is vacuum sealed to the main body with a viton high temperature O-ring. The vacuum chamber has two windows to allow a light path through the specimen enabling photoelastic measurements to be made. These measurements are made on soda-lime glass to ensure that the stress field in the disc is as theoretically predicted. The two other ports lead to the vacuum pump and the cylinder of dry nitrogen (used to provide an inert atmosphere). A strip of asbestos paper was applied to the anvil surface with heat sink paste for each test. This acted as padding for the specimens which were in the form of discs 15 mm in diameter and 3 mm thick. The whole assembly was built on an Instron universal testing machine which was used to apply and monitor the load.
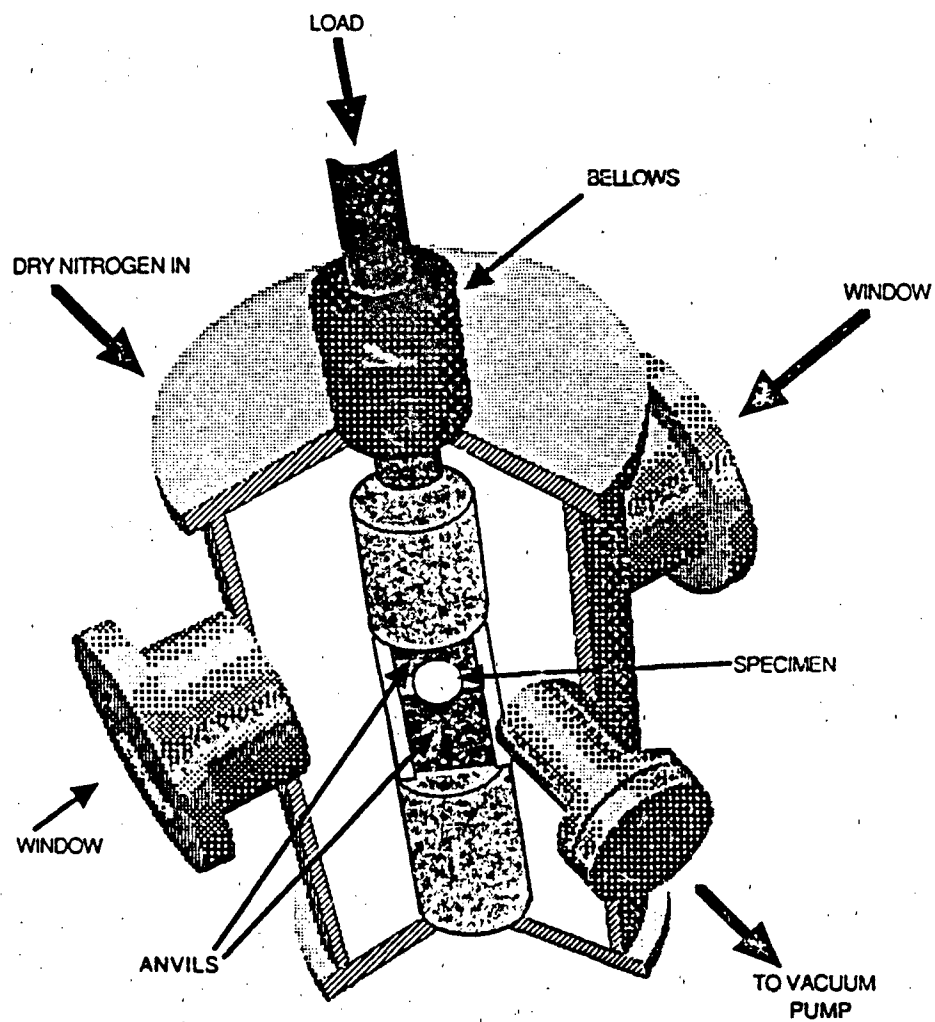
Figure 17

The Brazilian test apparatus and
surrounding environmental chamber.
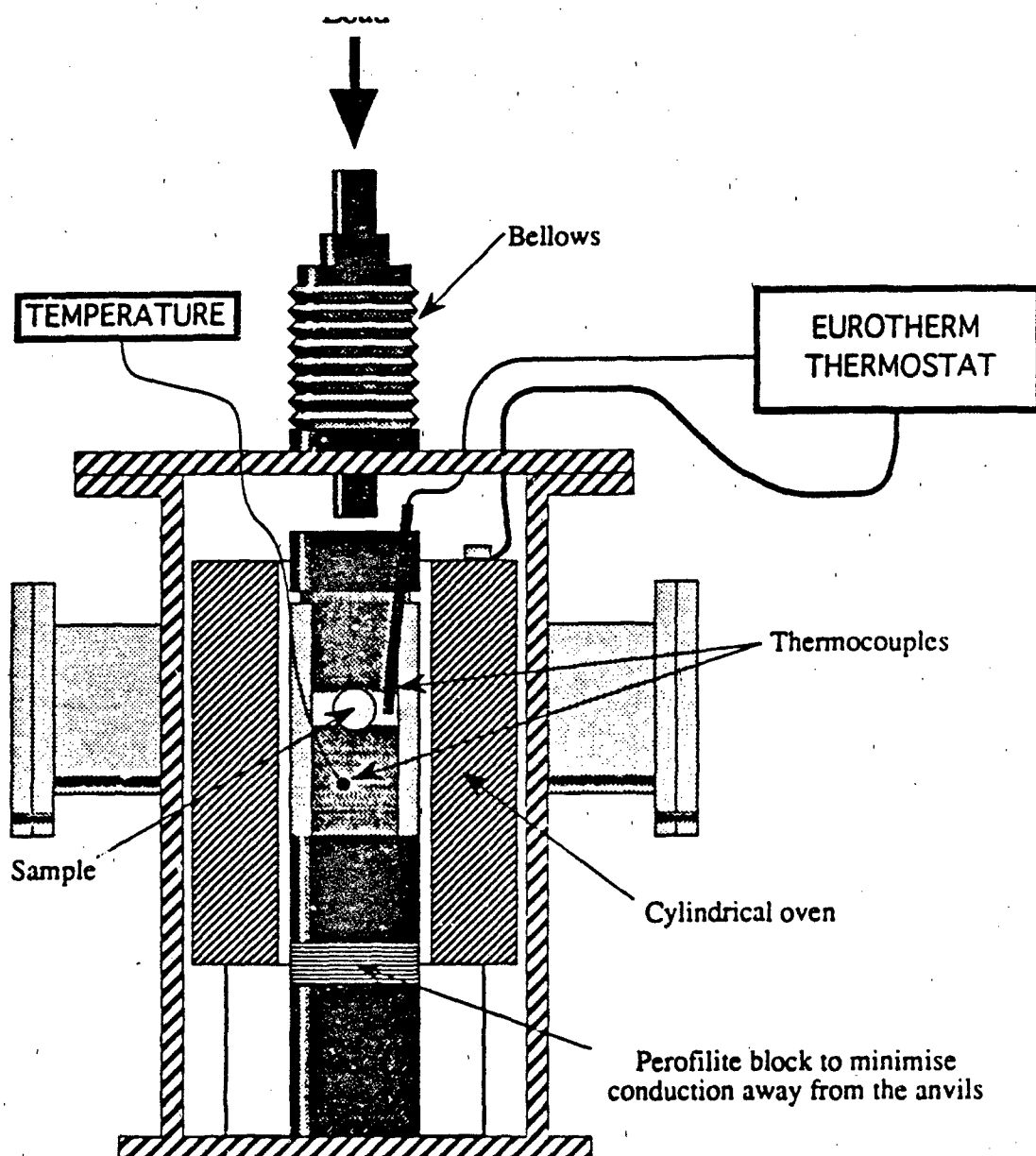
Figure 18

Brazilian test apparatus for elevated
temperature experiments in an inert
atmosphere.
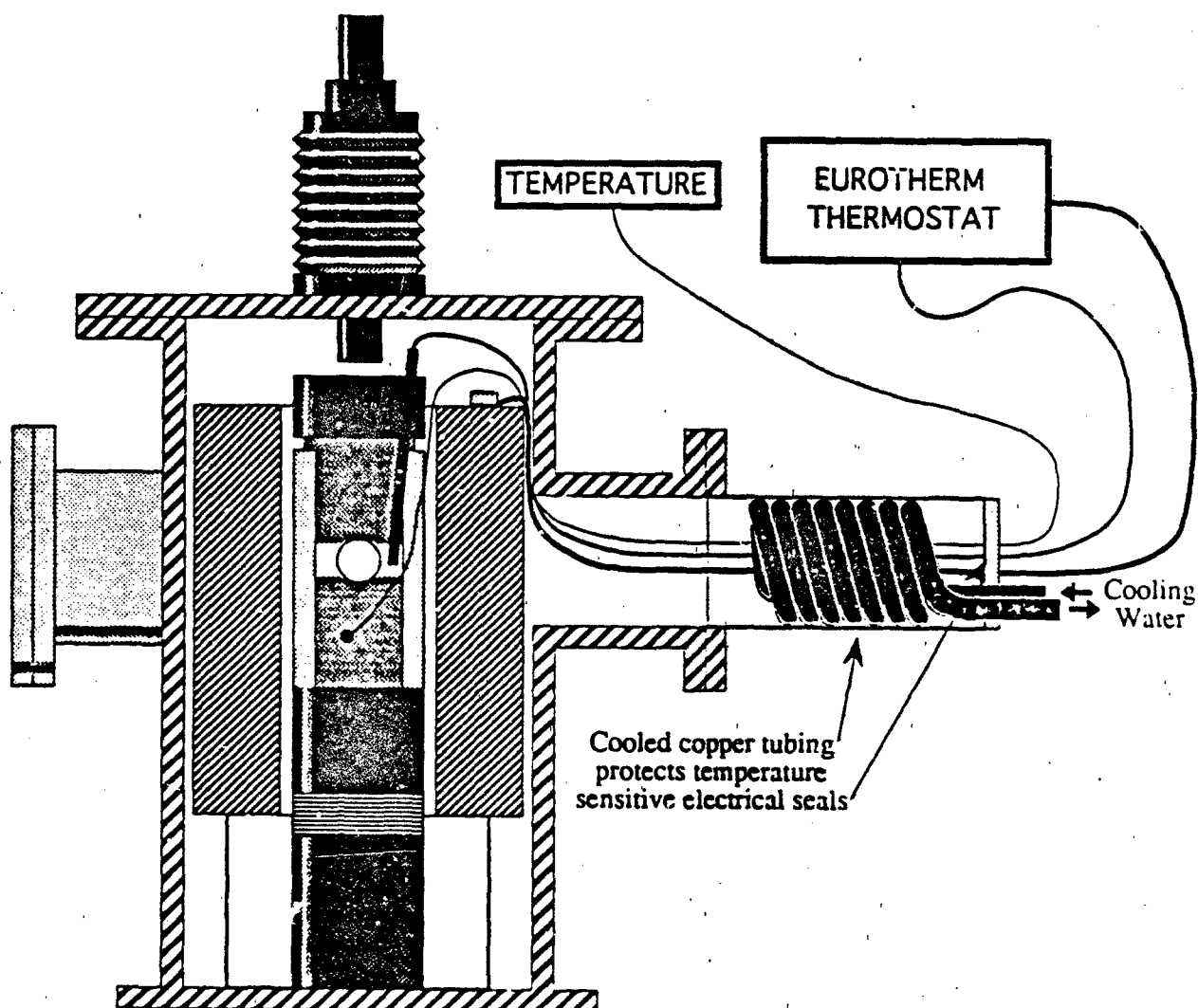
Figure 19
Modification to the Brazilian test apparatus
to increase the upper temperature limit.

TEMPERATURE

EUROTHERM THERMOSTAT

Cryogenic solenoid

Liquid nitrogen

Copper tubing

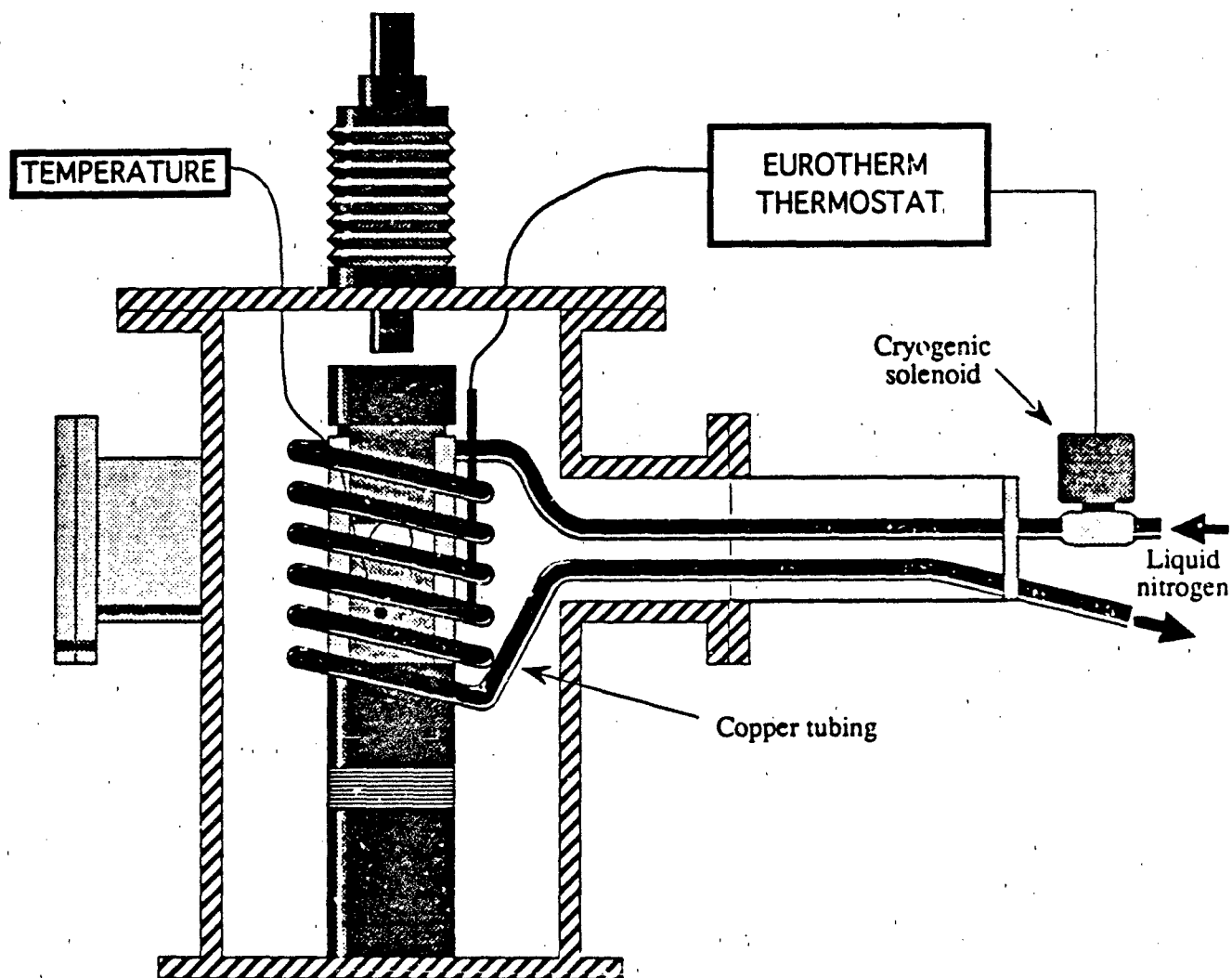**Figure 20**

Brazilian test apparatus for low temperature
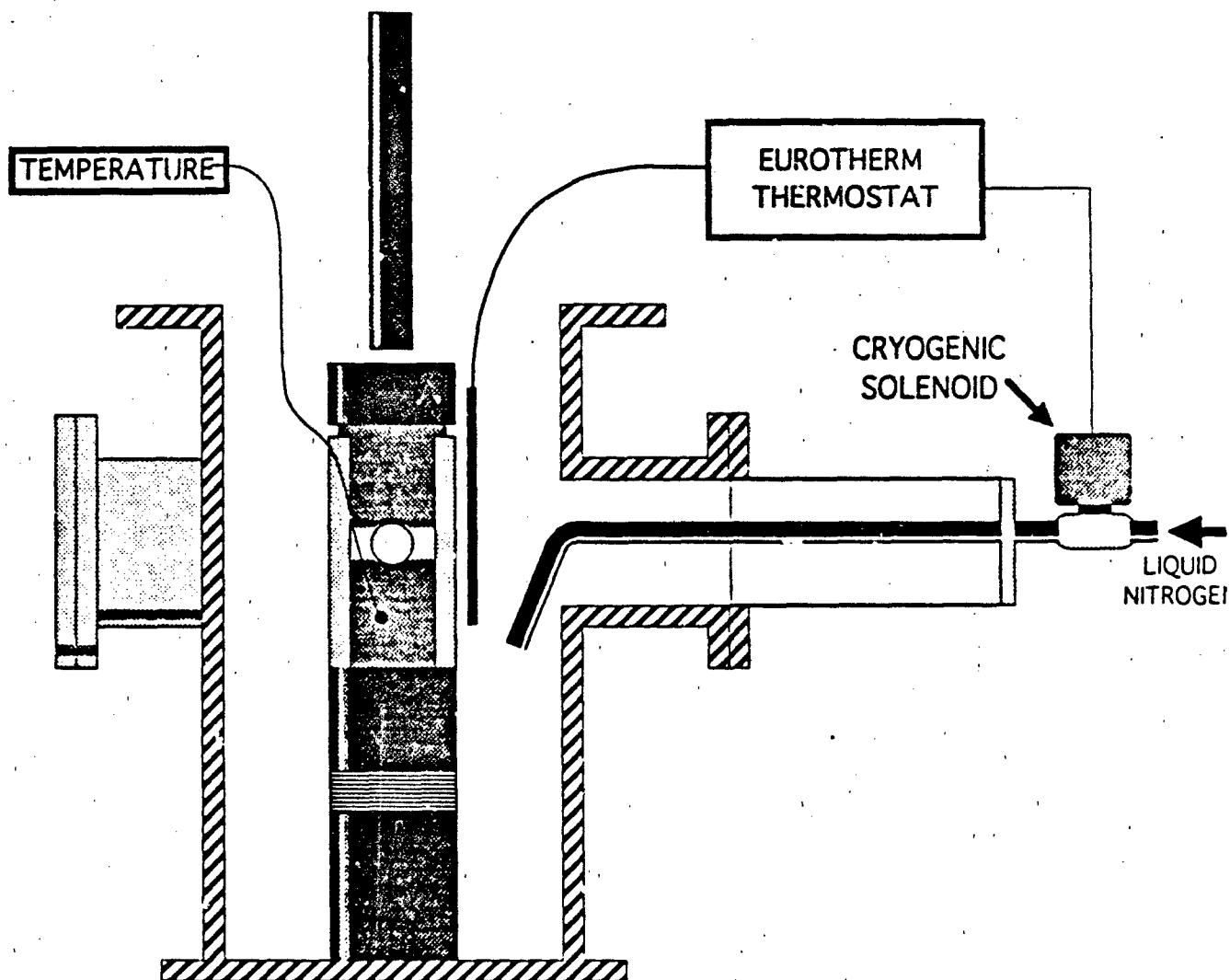experiments in an inert atmosphere.

Figure 21
Simplification of the low temperature
Brazilian test apparatus for experiments in
the laboratory atmosphere.

3.3.2 Environment

The experiment was to be performed in an inert environment since zinc sulphide is susceptible to oxidation at high temperatures (Prabhu et al., 1984) and also to reduce the effects of stress corrosion due to moisture in the air (although there will still be water adsorbed on the specimen surfaces). In order to achieve this, the chamber was connected to a vacuum pump and a cylinder of high purity dry nitrogen (white spot oxygen free dry nitrogen < 2 parts water per million by volume). A preliminary investigation with a hair hygrometer, showed that the relative humidity in the chamber could rapidly be reduced to ~5% at room temperature, by evacuating the chamber to a vacuum of ~0.1 Torr and flushing it with the inert gas and then repeating this cycle again. The sample was fractured in the nitrogen atmosphere at a pressure of approximately 1.2 atmospheres to ensure that if there were any undetected leaks, gas would escape rather than enter.

3.3.3 Temperature control

The temperature of the sample was raised by surrounding the central column with a cylindrical oven shown in Figure 18. The oven was controlled by a Eurotherm thermostat connected to a k-type thermocouple which was mounted in the test chamber. This arrangement sampled the gas temperature, and gave rapid feedback, while a second thermocouple monitored the temperature of the lower anvil.

For very high temperatures ($\geq 500\,°C$) a small modification had to be incorporated into the apparatus to protect the vulnerable connections where the thermocouple and electrical wires penetrated the chamber (see Figure 19). This protection was achieved by removing one of the windows and replacing it with a water cooled tube. In this way the electrical connections at the end of this tube were isolated from the high temperatures.

Lower temperatures were obtained by replacing the oven with coils of copper pipe, shown schematically in Figure 20. The evaporation of liquid nitrogen (boiling point 77 K) in a sealed container provided sufficient pressure to force the liquid through the coils. The flow was regulated by a cryogenic solenoid, which was in turn controlled by a Eurotherm low temperature thermostat. The thermocouple system was identical to that described above.

Figure 21 shows the final configuration used for temperature control. This simplification of the low temperature geometry was used for the germanium tests since they were tested

in a laboratory atmosphere. The temperature was controlled by simply allowing the chamber to fill with boiling liquid nitrogen vapour.

In all cases calibration was achieved by performing a dummy run with an instrumented sample and allowing time for its temperature to equilibrate (the temperature control being accurate to within 5 °C). After the high temperature test the specimens were allowed to cool down to below 200 °C in the inert atmosphere to prevent any oxidation.

3.4   RESULTS

3.4.1.   The High Temperature Fracture Stress of Germanium

The graph shown in Figure 22 gives the results of Brazilian tests performed on Germanium samples from two different sources at three different temperatures. The samples from source A were monocrystalline, while those from source B were polycrystalline but with large grains (typically 5 mm).
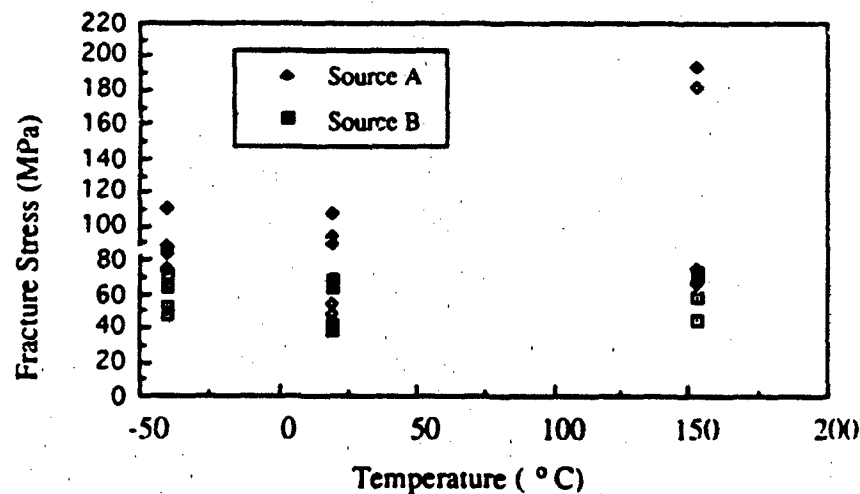
Figure 22
The fracture stress of germanium
as a function of temperature.

The data show a wide spread which appears almost bimodal in nature, especially at high temperature, due to the crystallinity of the material (since the geometry has only one tension axis it is very sensitive to the orientation of the sample). The baseline results from 25 mm diameter 2.5 mm thick discs in the hydraulic burst test were 111 ± 18 MPa for material A and 92 ± 16 MPa for material B. These data do not show the bimodal

30

distribution in the results because, in contrast to the Brazilian test, the axisymmetric burst test samples the flaws equally regardless of orientation.

Despite the spread in the Brazilian test data it is clear that the fracture stress increases at 153 °C and to a far lesser extent at -40 °C and that the strength of the material from source A is higher than that from source B. The temperature dependent fracture stress variation could be explained by the removal of water from the atmosphere at the upper and lower temperatures which reduces the effects of stress corrosion. Since the loading rate is quite slow (approximately 15 s) there is time for stress corrosion to affect the results.

It is interesting to directly compare the room temperature results for the Brazilian and burst tests. For material A, the Brazilian test results have an average value 66% of those from the burst test, while for material B the factor is 61%. This comparison does not take into account the enhanced effect of orientation in the former test, but the close agreement with Hand's (1987) estimate of the same factor (65%) suggests that despite the reservations expressed in Section 3.2.1 the Brazilian test is generating reproducible fracture stress data.

3.4.2 The High Temperature Fracture Stress of Zinc Sulphide

It was possible to add more detail to the graph for zinc sulphide as more samples were available. Because of the spread in fracture stress due to the natural flaw distribution in the material, each point on the graph in Figure 23 is actually the average of ten samples, and the error bars show the standard deviation of the mean. The quantity of samples available allowed small variations in fracture stress to be investigated with some precision.

The room temperature value of 52.7 MPa is approximately 77% of the baseline value obtained by the bursting disc geometry (Matthewson and Field, 1980), 67 MPa. Taking into account the large spread in data in the latter experiment (25%) this value is again in good agreement with the estimate of Hand (1987).

For design purposes the most important feature of the graph is that within the temperature range -35 °C to 600 °C the average fracture stress never falls below its value at room temperature. In fact, as with germanium, the strength of the material initially increases with temperature, the graph having its first peak at 100 °C and then a second at 300 °C. It should be noted that the raw data shown in Figure 24 indicate that
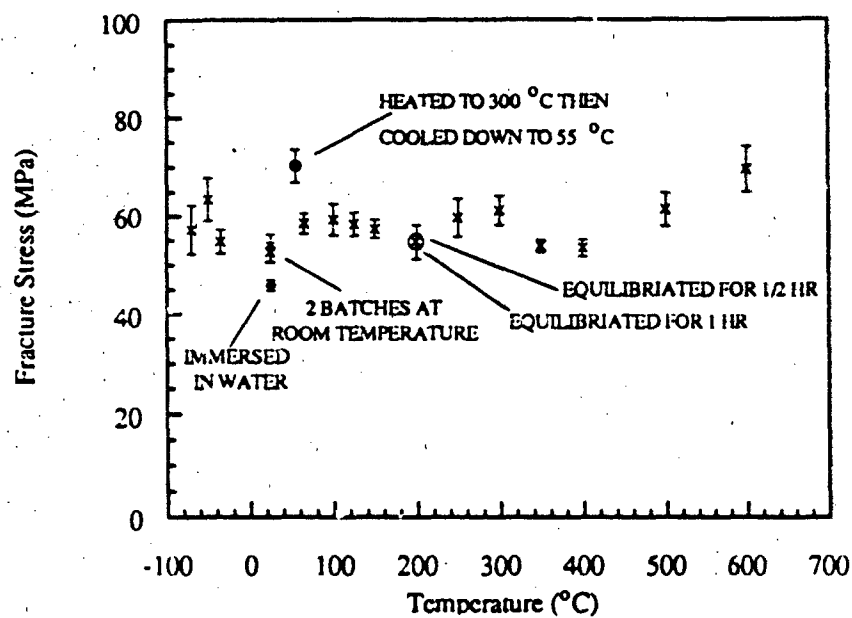
31

Figure 23
The average and error in the mean of
the fracture stress of zinc sulphide
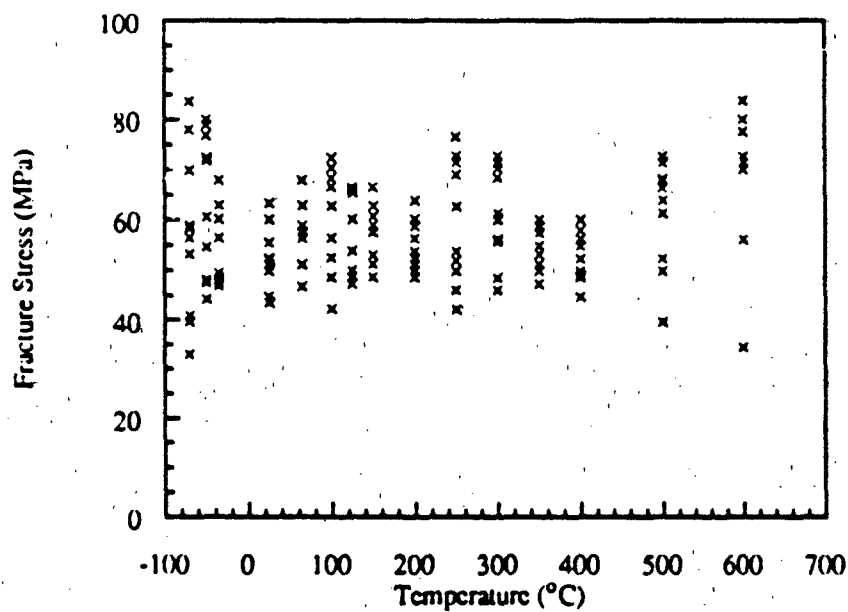as a function of temperature.

Figure 24
The fracture stress of zinc sulphide
as a function of temperature.

even though the average fracture stress is increased there is a greater spread in data at these peaks. For zinc sulphide, as with germanium, the assumption is that, as water is removed from the surface of the specimen, there is less water available at the crack tip. The effect of stress corrosion is therefore reduced and the flaws in the material will not propagate until the critical stress intensity factor is reached. Several other factors that could contribute to the variation in fracture stress were considered.

In order to minimise the time taken for the experiments, for those samples broken between room temperature and 200 °C the temperature was only allowed to equilibrate for half an hour, while for temperatures above this, the specimen was equilibrated for a full hour. Since this change in the experimental conditions occurred at a temperature at which there was also a sudden change in fracture stress, it was decided to repeat the experiment at 200 °C with an equilibration time of one hour, to see if this change in heating time affects the results. The closeness of the results for the two different conditions indicated in Figure 23 shows not only that the discrepancy in the heating times was not the cause of the increase in fracture stress, but also that the test was very reproducible.

The increase in fracture stress at 300 °C might have been caused by a permanent chemical change at the elevated temperature. This possibility was eliminated by comparing the infrared transmission spectrum from a specimen that had been heated to 400 °C and then cooled, with the spectrum from an unheated specimen. Figure 25 shows that the two traces differ only in absolute magnitude, which is due to the nature of the measurement rather than to a change in the material.
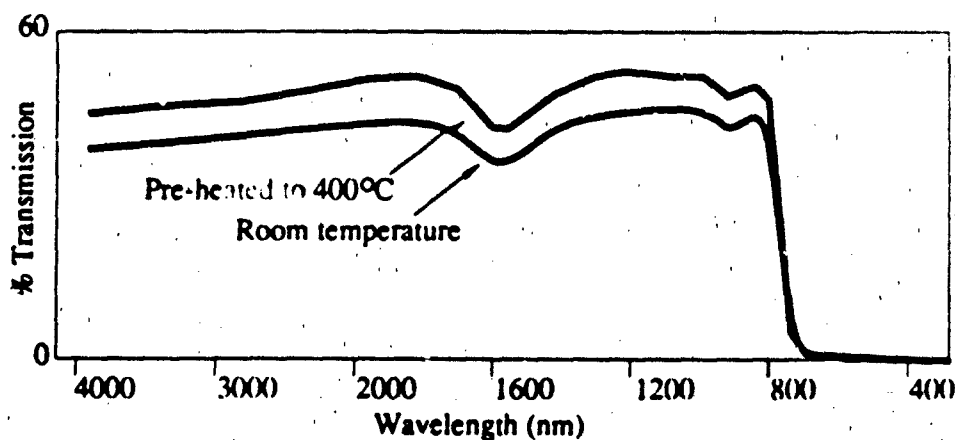

Figure 25

The infrared transmission spectrum of zinc sulphide.

Ten specimens were heated up to 300 °C and then allowed to cool under vacuum over a period of about 4 hours before being loaded. The result of these experiments was an increase in average fracture stress to 70 MPa which is higher than the value at room temperature (52 MPa) and that at 300 °C (61 MPa) (Figure 23). These results support the stress corrosion hypothesis, since the prolonged heating cycle and vacuum conditions both reduce the amount of atmospheric and adsorbed water further and thus raise the fracture stress.

It was therefore predicted that a sequence of experiments performed at room temperature with the specimen fully immersed in water would display a reduction in strength. The point indicated in Figure 23 shows that this is indeed the case and emphasises the environmental effect on the strength of zinc sulphide.

The samples provided for the low temperature experiments were from a different batch of zinc sulphide, and appeared noticeably paler than those for the high temperature experiments. The room temperature results were, therefore, repeated for the second batch and compared with those for the first batch. The two values are identical to within 2%, again verifying the reproducibility of the test. The low temperature results, taken at -35 °C, -50 °C and -70 °C showed a slight increase in strength, which would again be explained by a reduction in the effect of the stress corrosion mechanism.

3.4.3 High Temperature Strength Data on Zinc Sulphide from the Literature

Data on the high temperature strength of zinc sulphide are very scarce. One set was presented by Schwartz at the IR workshop in 1990 and shows a steady increase in strength with temperature. Further evidence for this can be found in Deom et al. (1990) in which a value of flexural strength for zinc sulphide is given as 104 MPa at 25 °C and 152 MPa at 500 °C.

An earlier experiment, again using the Brazilian geometry, by Hand (1987), although suffering from a limited number of specimens and hence a large inaccuracy in the mean of the data, produced a graph the shape of which is similar to that obtained in this study, and suggested a slight decrease in strength at 700 °C accompanied by evidence of plasticity. This fracture stress reduction with plasticity is characteristic of high temperature strength data on ceramics (Davidge, 1979; Shinkai et al., 1981). Using the same test geometry, the variation of fracture toughness with temperature was determined by indenting the

34

specimens prior to the experiment. The size of the flaw could be measured, and from this the fracture toughness (critical stress intensity factor) could be derived. The increase in strength with temperature that was observed in these tests was attributed partly to an anealing of residual stresses, and partly to water loss and crack tip blunting. Hand (1987) also assessed the variation of compressive strength with temperature and obtained a decrease with temperature similar to that observed in the Brazilian test data of the same study. The drawing of conclusions from this last set of results is, however, hindered by the change in failure mode at higher temperatures due to the change in compliance of the anvils.

A low temperature result was mentioned in Section 2.7 from the paper by Wahl and Tustison (1990), which showed no variation in strength between 77K and room temperature. This result was used as further evidence for their contention that zinc sulphide is resistant to stress corrosion.

3.4.4   Analysis

The apparent discrepancy between the various sources of high temperature data can be explained by the difference in the experimental conditions. Experiments carried out in a nitrogen environment show a minimal rise in strength with temperature. Those carried out in air show a steady increase. The increase can therefore be attributed to crack tip blunting by oxidation (Prabhu et al., 1984; Davidge, 1979) and by the reduction in the amount of adsorbed water.

The mechanisms for the slight variations in the results of the present study are more difficult to discern. Xue and Raj presented results that suggest that intergranular cavitation and grain growth are minimal at temperatures below 950 $^{\circ}$C. Crack blunting through dissolution in, and reprecipitation from, atmospheric and adsorbed water has been discussed at length for glass (Ikeda et al., 1990; Han and Tomozawa, 1989; Hirao and Tomozawa, 1987). There seems, however, to be very little reaction between zinc sulphide and water at these low temperatures (Brion, 1980; Sohn and Daesoo, 1987).

For the reasons given above the variations in strength are most likely to be due to the effects of stress corrosion varying with the amount of adsorbed water. This would explain the increase up to 100 $^{\circ}$C and, because water can remain adsorbed up to quite high temperatures (Holland, 1964), could possibly explain the increase at 300 $^{\circ}$C. It is difficult to detect the removal of such a thin layer of adsorbed water through calorimetry. (Hand,

1987) but the increase in strength when allowing the sample to cool in a vacuum, and the reduction in strength when the sample is immersed in water lend credence to this hypothesis. Section 2.2.1 indicated that stress corrosion and crack growth are thermally activated phenomena and an increase in temperature can therefore decrease the fracture strength. This complication means that it is very difficult to accurately predict the shape of the graph through this mechanism.
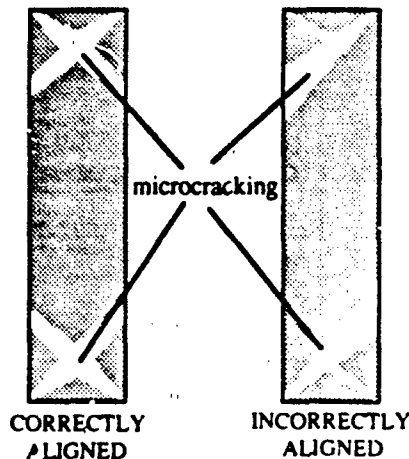

CORRECTLY
ALIGNED

INCORRECTLY
ALIGNED

Figure 26

Areas of microcracking in
Brazilian test specimens.

Hand (1987) detected plastic deformation at 700 °C which is quite low considering the fact that the melting point of zinc sulphide is 1830 °C. The tendency for the fracture stress to increase above 500 °C in the present study could be explained by the onset of plasticity causing increased crack rounding. It is evident, however, that there is a slight change in the failure mode at these high temperatures since microcracking (Hand, 1987) can be observed within the bulk of the material near the loading points. These whitened areas in a cross-section down the loading axis (the plane of the primary crack) are shown in Figure 26 for both a correctly aligned and incorrectly aligned specimen.

It is difficult to attach any significance to the variation in the spread in the data at 100 °C, 300 °C, 600 °C and at low temperatures because the error in the error is always large and, particularly in the last two cases, the quality of the samples was poor: liquid impact patterns from the batches tested at 500 °C, 600 °C and -70 °C show the familiar long linear cracks indicative of poor surface finish superimposed on the characteristic short circumferential liquid impact cracks. Earlier batches showed a far more typical pattern.

3.5 CONCLUSIONS

These experiments have demonstrated that in the normal operating temperature range the room temperature value of the fracture stress is a safe parameter to use for design purposes. The fracture stress of germanium also remains above the room temperature value at the experimental temperatures.

In an air environment it appears that the fracture stress of zinc sulphide actually increases with temperature as does its rain erosion resistance (Hand, 1987; Deom et al., 1990). It would not, however, be prudent of the missile designer to rely on this increase since its mechanism is not well understood.

At high temperatures (≥ 600 °C) there is evidence of microcracking and plasticity in zinc sulphide. This may suggest that above these temperatures the material's strength is severely compromised.

4   STRENGTH TESTS ON LARGE ZINC SULPHIDE DISCS

4.1   FRACTURE STRESS RESULTS

Seven large ZnS discs (125 mm diameter by 5.45 mm) were supplied by British Aerospace and were tested in the hydraulic busting disc apparatus (Matthewson and Field, 1980). The discs were from different batches and two (discs 6 and 7) were noticeably darker and had obvious streaks within the bulk of the material (see Figure 27) which correlated with distortions in the bubble structure. In addition careful inspection of the surfaces revealed areas where faint grinding and polishing marks were visible. The fracture stress results are given in Table 1 which also includes the stress at the centre of the disc (where it is a maximum) at the time of failure. The lowest stress was 55.9 MPa which failed at a distance of 30 mm from the centre which means that the central region survived a stress of 79 MPa. The remaining specimens all fractured within 25 mm of the centre and there were no edge failures. The highest fracture stress was 98 MPa and this was achieved by one of the dark specimens. The second dark specimen also had a high stress 97.6 MPa (the highest fracture stress of a lighter coloured sample was only 88.8 MPa). However the small number of samples makes it difficult to estimate the significance of the fracture stress difference.
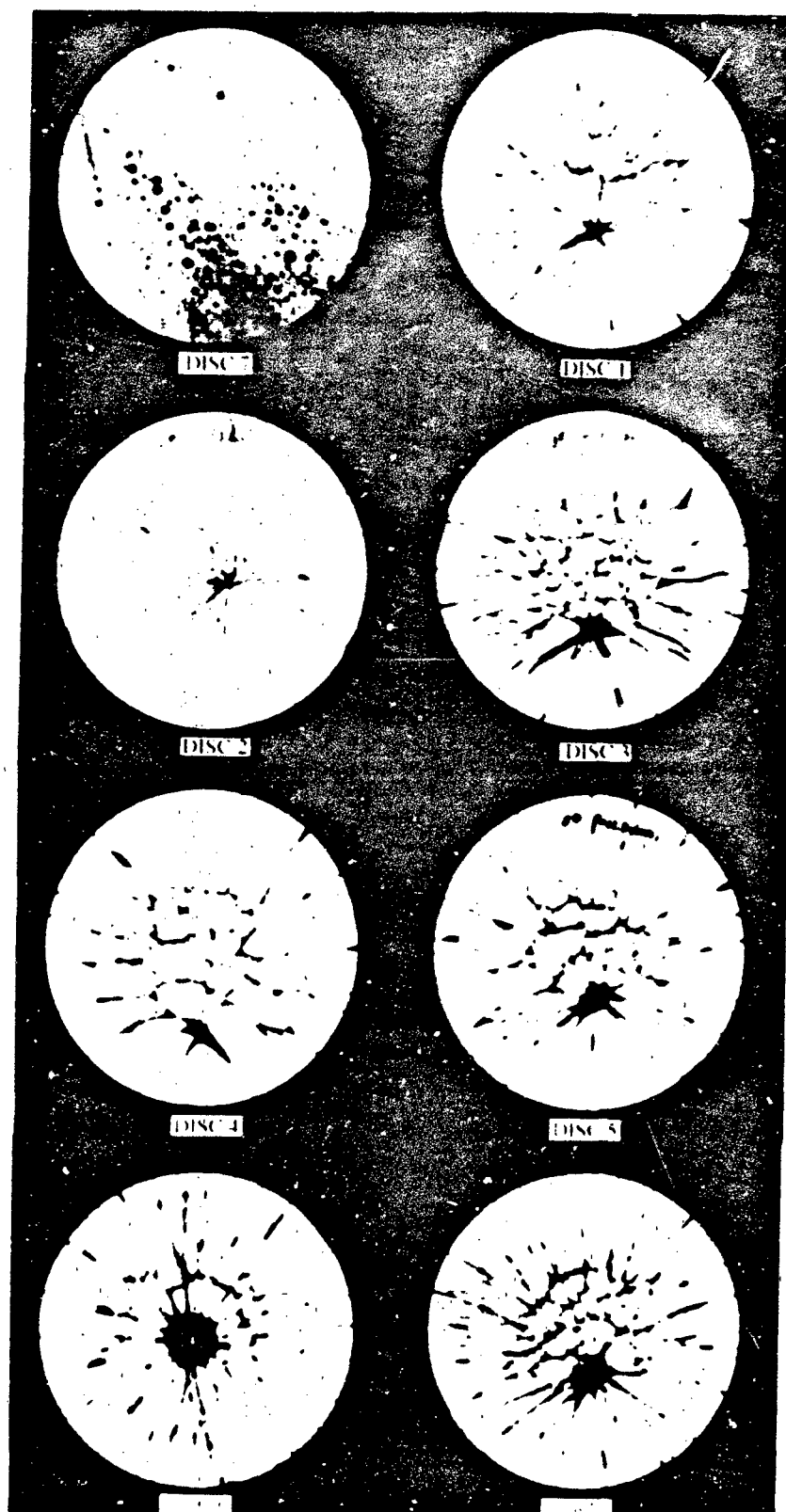
Figure 27

TABLE 1

	SPECIMEN CODE	FRACTURE STRESS (MPa)	STRESS AT DISC CENTRE (MPa)	COMMENTS
1	PP88-20-2B	70.6	78.8	
2	PP88-09-4D	75.8	77.9	
3	PP88-09-5D	87.4	109.6	
4	PP88-20-2J	55.9	79.0	
5	PP88-09-3E	88.8	102.8	
6	PP88-09-2C	97.6	98.7	dark, streaks
7	PP88-09-2H	98.0	117.2	dark, streaks

4.2 CONCLUSIONS

The average fracture stress of the seven discs was 82 MPa with a standard deviation of 15.4 MPa. The two darker specimens appeared to exhibit higher strength despite the inhomogeneity in their structure. A previous report (Hand and Field, 1989) on discs of a similar size and various surface finishes produced results which are in good agreement with the present study. In this earlier test, three of the samples failed at high loads giving an average fracture stress of 85 ± 5 MPa. But of the remaining three samples there was one edge failure and the other two were noticeably weaker (30 ± 6 MPa). This was thought to be due to an inadequate surface finish. It appears that this is no longer a problem if the surface preparation is carefully controlled.

5 THE ROLE OF THE MULTIPLE IMPACT JET APPARATUS

In order to develop improved infra-red window materials the material scientists needs to evaluate:-

1. the threshold velocity for damage and
2. the rate of transmission loss once above this threshold

The Single Impact Jet Apparatus has up to now provided the standard way of evaluating the threshold velocity. To do this 25mm discs of the material under test are impacted in the centre 5 times and then the disc is broken in a bursting disc test to evaluate the residual strength. This is carried out at a number of different velocities and the results plotted on a graph of residual strength v velocity to discover the threshold velocity below which no drop in residual strength is observed from that of the unimpacted material. The test involves breaking about 20 discs of the material and the result is accurate to about 5-10% depending on the quality of the surface finish.

In the above experiment the discs must be broken because once above the threshold velocity there may be enough energy to extend the microcracks present, but after just 5 shots they may not have been extended enough to be detectable by visual inspection. The test thus relies on the fact that after 5 shots even if not big enough to see, the cracks under the impacted area if they have grown, are larger than those naturally occurring elsewhere on the specimen, and will thus reduce its strength. In a poorly polished material this will obviously not always be the case and a large scatter in the data occurs.

MIJA can eliminate the necessity to break the discs by impacting the site enough times to extend the cracks until they are visible. This means that a large number of test sites can be tried on one specimen and thus fewer discs are required to evaluate the threshold velocity. This is particularly important with expensive materials such as diamond.

In addition to this advantage MIJA offers a finer control of velocities (spread 1%) and actually measures the speed of every jet before it impacts. It also has a more finely controlled equivalent drop size because the nozzle is filled more reproducibly for each shot than is possible for SIJA. Together these improvements result in a test that can locate the threshold velocity to 1-2%.

Erosion data on the rate of transmission loss above the threshold velocity has previously required the use of whirling arm rigs. The problem with such test rigs is that the drops entering the chamber become distorted by the turbulence generated by the whirling action of the arm. The drops impacting the specimen are thus distorted so they have a range of contact radii and result in damage of varying sizes many showing the presence of voids. This range of effective drop diameters is rig dependent thus making comparison of results between rigs difficult. A solution to this problem used in some rigs is to reduce the chamber pressure, however this has resulted in a range of pressures now being in use each producing a different rise in specimen temperature on rotation.

In contrast to the above, MIJA can impact at a selected site, at a measured velocity with a reproducible front profile to the jet. This allows identical experiments to be performed on materials, even down to the order of impact sites in a random pattern, and thus true comparison of material erosion behaviour is possible. The major disadvantage is the number of shots required for such an experiment. As MIJA only fires a shot every 2 seconds the experiment times maybe longer than with a whirling arm rig, however since MIJA can choose to impact over a smaller area and can be left firing under computer control the duration of a test is not so critical, and the advantages of reproducibility are worth the wait.

SPECIFICATIONS

Number of shots a minute	30
Velocity range	30 - 5?? m s^{-1}
Drop diameters simulated	3 - 8 mm
Positional accuracy	25 μr.

Impact positions and velocities can be defined by the user, allowing shots to be fired on one site, on a line, in an array, randomly over an area or in a user-defined pattern.

MIJA is fully automated and includes:
    computer control of the firing sequence
    database of specimen specifications
    storage of position, velocity and time of each shot fired in an experiment
    analysis of the above stored data

Note: Testing on nozzle design is still continuing and this will effect the equivalent drop size of the jets produced. Care must therefore be taken in comparisons of results with the single impact gun and other MIJA results. It is hoped that a final nozzle design and new equivalent drop curves for it will be finalised within 6 months.

5.1 THRESHOLD VELOCITY RESULTS FOR GeC ON ZnS

In this test MIJA was used to evaluate the threshold velocity for GeC coated ZnS by impacting a site 30 times at a given velocity and then assessing the site for damage. If one of the shots fired on the site has enough energy to open up a microcrack then subsequent shots should extend the damage until it becomes visible. The exact number of shots required to make this test work properly is not yet known, although the 30 shots used in this experiment gave a high degree of reproducibility. A probability of survival can be calculated for the material based on the number of sites showing damage after impact at a given velocity, this probability will drop to zero as the velocity increases beyond the damage threshold.

The material tested in this example was Plessey PPZ-23. On each of three specimens 56 sites were impacted and subsequently evaluated for damage, the resulting data is from a total of 122 sites for the well-bonded specimens and 166 sites for the poorly bonded. Each site was impacted 30 times with a typical velocity spread of between 3 and 5%. The maximum velocity fired on each site was recorded and damage was then looked for. Between each of the 56 experiments on different impact sites the firing pressure was increased which meant that as far as possible subsequent impact sites had a higher maximum velocity. Impact sites were placed on the specimen in a way that we could be sure that damage visible on a particular site could be attributed to the jet impacts that occurred there.

The results obtained are displayed in Figures 28 and 29 for the well bonded and poorly bonded coatings respectively. The bar chart on each graph shows the number of sites with a maximum velocity of V m s^{-1} and the scatter graph the corresponding probability of survival at that velocity.

The two batches of specimens both have the same starting value to the probability of survival decrease. The samples where the coating is less well bonded appear however to offer reduced protection at higher velocities ie the velocity range is 130 - 153 m s^{-1} for the well bonded coating and 130 - 145 m s^{-1} for the poorly bonded coating. This might be because the poorly bonded coating protects for a smaller number of the 30 shots than the well bonded, but further experiments will be necessary to ascertain this and to impact the substrate and make sure that the threshold velocity for the coated ZnS is actually higher than the uncoated and that the GeC hasn't put the surface into tension on its application. The improvement in threshold velocity afforded by the addition of the coating is marginal.
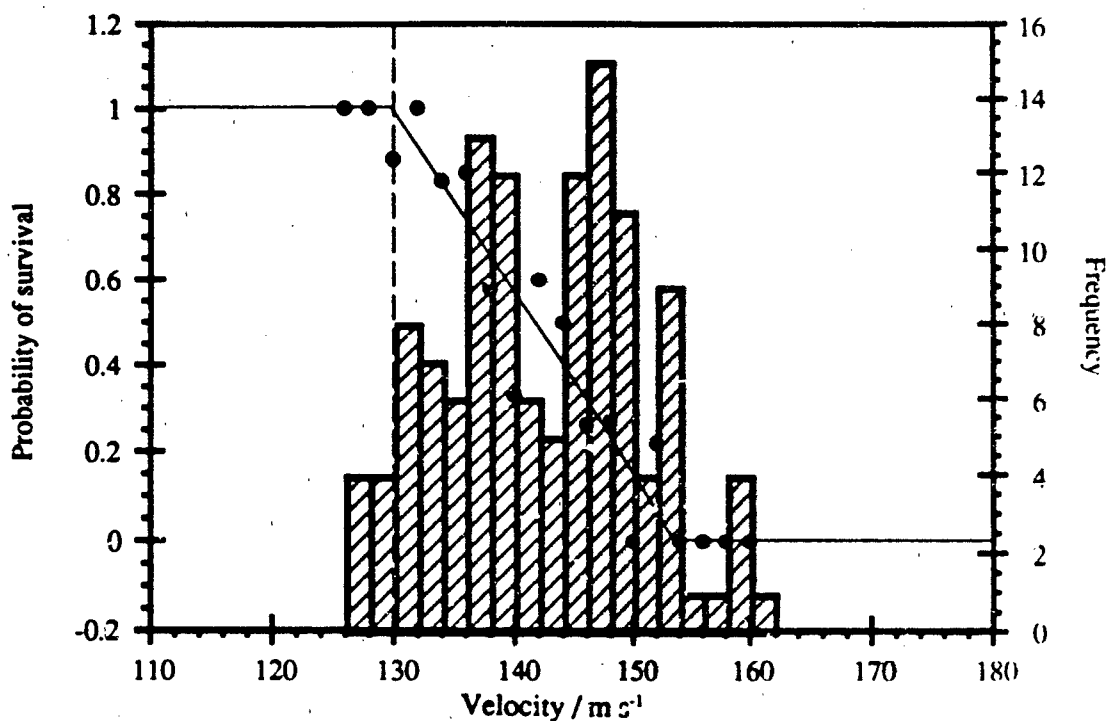
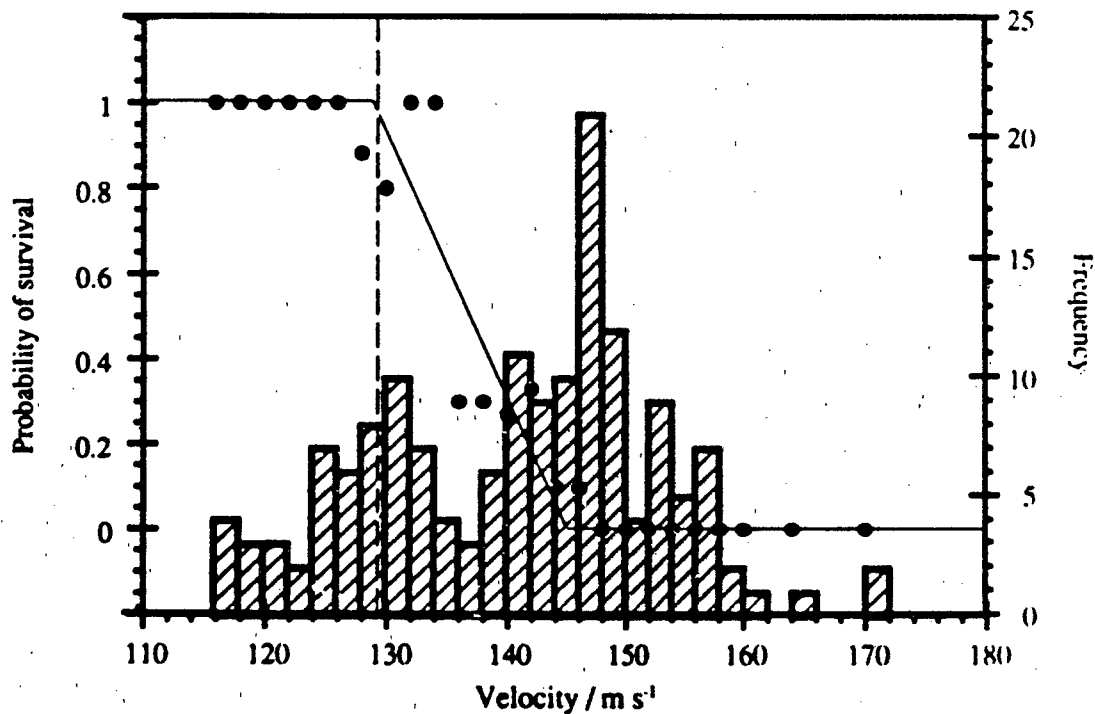**Figure 28** Plessey ZnS coated with GeC - well bonded specimens

Figure 29 Plessey ZnS coated with GeC - poorly bonded specimens

6 EXPERIMENTAL TECHNIQUES

6.1 THE BRITISH AEROSPACE THERMAL SHOCK RIG

There has long been a need for a standardised thermal shock test that can order a wide range of materials in terms of their resistance to a thermal shock environment. The severity of a particular shock event depends critically on many parameters (Kingery, 1955), such as specimen, size, shape, strength, modulus, surface finish and thermal properties and the heat transfer rates inflicted by the environment. Many of these factors are highly dependent on the varying temperature and the ordering of materials can be very different under different thermal shock conditions. The most obvious example of this is the strong dependence on whether the event is one of rapid cooling (downshock) or heating (upshock). It is therefore vital to design the standard test conditions to be as close to those experienced by a specimen in the real situation that it is designed to survive.

The situation in this case is that of a front window of a missile experiencing rapid aerodynamic heating as it accelerates towards its target and the BAe rig shows some promise in that it provides a temporal heating profile that is similar to that inflicted on the window. The failure of a specimen is, however, also highly dependant on the *spatial* heating profile.

The thermal shock rig was designed and built by British Aerospace in Stevenage (Graham et al., 1990) and is shown in Figure 30. The apparatus consists of four tungsten-quartz lamps within a section of a polished, silver-coated sphere which integrates the light energy from the bulbs and projects it through an aperture in the sphere onto the surface of the 25 mm disc sample. The number of bulbs lit can be selected and in addition the power level of one of the bulbs is continuously variable. The temporal power variation has been shaped electronically to reduce the heating rate in the first 1.5 s. This is achieved by switching the power on and off rapidly during this time and has the effect of producing a heating rate that more closely approximates that experienced by a missile.

The surface of the sample is blackened to improve its absorptivity. For low temperature experiments this is simply achieved by coating the surface in candle soot. At temperatures in excess of 500 °C, however, the carbon in the soot oxidises and a high temperature paint must be used. Once painted the sample is baked to prevent the paint outgassing during testing and contaminating the sphere. The paint has the disadvantages that it is difficult to remove after the test, it begins to deteriorate above 650 °C and does not fully absorb the incident radiation but there is, as yet, no satisfactory alternative.

ADVANTAGES

1.   **The Thermal Shock is Reproducible.**

2.   **The Apparatus is Easily Portable.**

3.   **The Geometry is Ostensibly Easy to Simulate Theoretically.**

4.   **The Apparatus is Cheap.**

5.   **The Technique is Flexible.** The profile of the thermal shock can be shaped both temporally (by adjusting the power to the bulbs) and spatially (by masking areas of the disc).

DISADVANTAGES

1.   **The Heating Profile is Not Axisymmetric.** This complicates the theoretical analysis of the technique. This can be overcome by, for instance, spinning the disc.

2.   **The Test is of Low Severity.** The prototype is unable to cause the full range of materials of interest to fail. The severity can be increased by masking areas of the disk and by reducing the disk thickness.

3.   **The Severity Depends on the Absorptivity of the Test Material.** The paint does not completely absorb the incident radiation and the amount of heating experienced by the sample therefore depends on its opacity to the incident radiation. This factor does not affect the thermal shock resistance of an accelerating missile window and the test will therefore give an ordering of materials which is not representative of their ability to survive in the real situation.

Clearly the prototype and the experimental procedure must be modified to allow the technique to realise its potential as a universal method for ordering materials in terms of their thermal upshock capabilities.
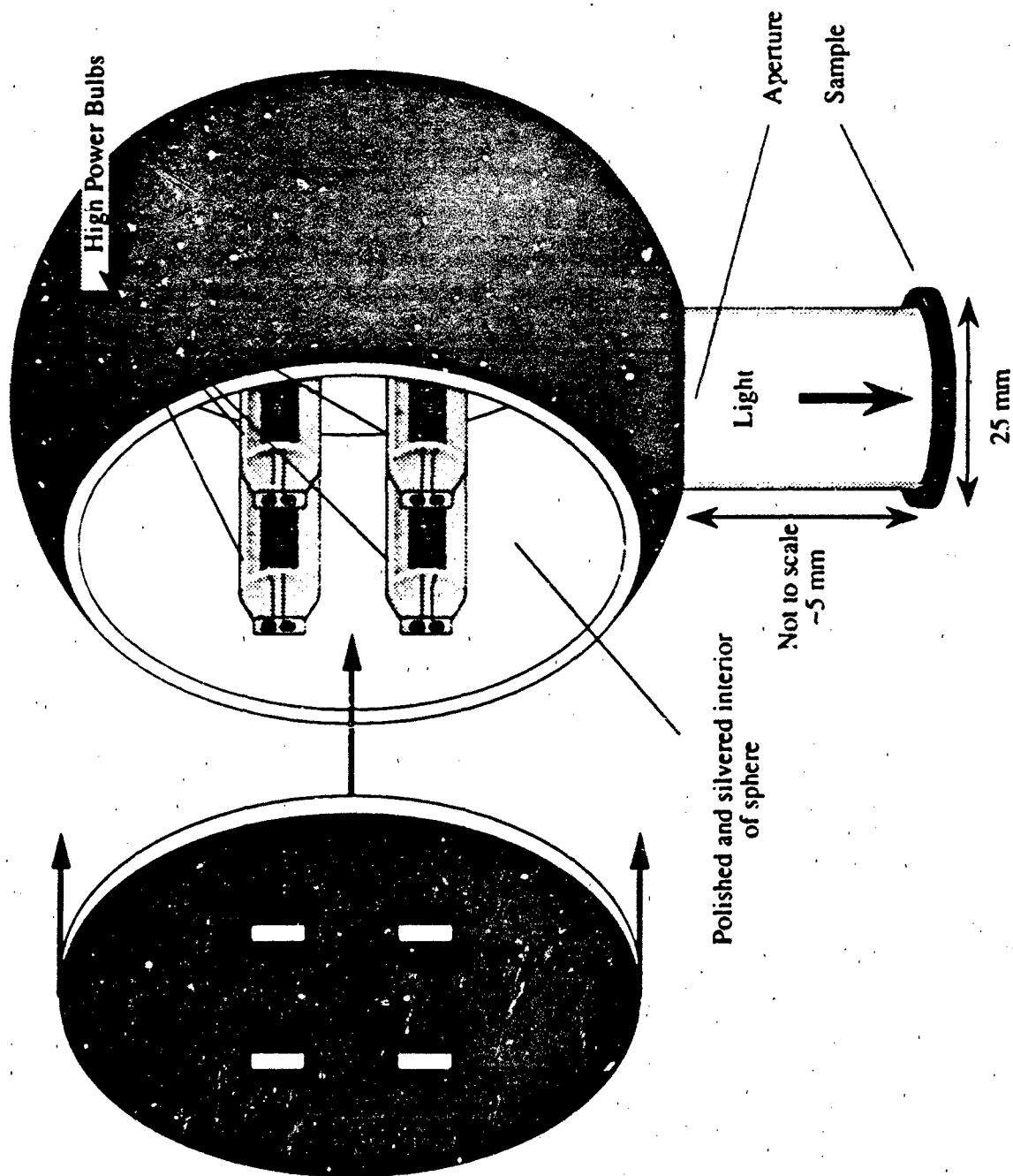
High Power Bulbs

Aperture

Sample

Light

2.5 mm

Polished and silvered interior
of sphere

Not to scale
~5 mm

Figure 30
The interior of the British Aerospace
Thermal Shock Rig.

6.2 MEASUREMENT OF THERMAL AND MECHANICAL PROPERTIES FOR THIN LAYER PROTECTIVE COATINGS FOR IR MATERIALS

The thin films under investigation are, diamond, germanium carbide and boron phosphide.These are prospective protective films for infra red transparent window materials. Their purpose being to increase the useful life of the window by reducing damage caused by rain and solid particle erosion. In service these materials may be subjected to temperatures as high as 900°C, so a high temperature rig was set up which allows the properties to be measured in an inert atmosphere, at any temperature from room temperature to 900°C.

The film properties of greatest interest are the Young's modulus, thermal expansion , thermal conductivity and internal stress. The Young's modulus is an important thin film property as it provides a great deal of information about the nature of thin films, most importantly how they differ from the corresponding bulk material. Variation of modulus for a given film type may reflect differences in crystallinity, orientation and quality of the film. Techniques for the measurement of Young's modulus include the vibrating reed, Brillouin scattering, bulge test and micromechanical indenter, of which the vibrating reed and bulge test were selected for further study. The vibrating reed is a dynamic technique which allows the Young's modulus of a film to be determined by measurement of the natural, or resonant frequency of vibration of a specimen clamped at one end, when vibration is induced electrostatically. For simple sample geometries the natural frequency of vibration can be directly related to the modulus of the sample. The modulus is calculated by exciting the sample into vibration. Vibration of the beam is achieved by applying an alternating electrostatic field across the capacitor formed by the beam and the reference electrode. When the frequency of the excited signal equals that of the resonant frequency of the beam, the amplitude of vibration passes though a maximum. Since the beams are electrostatically attracted towards the substrate with either voltage polarity, the frequency of the excited mechanical motion is twice the applied electrical frequency. The modulus of thin films are usually measured using film/substrate composite beams, as this technique is not suitable for determining the modulus of substrate free films, unless the films are completely flat. The use of a composite beam allows the modulus of deposited films as thin as a few hundred angstroms to be determined. The resonant frequency of the substrate material (monolithic beam) is determined first. Then the experiment is repeated for the composite beam. It is from the shift in resonant frequency that the Young's modulus of the film is calculated. Room temperature Young's modulus values were calculated for silicon (161GPa). germanium carbide (255 GPa) and MPACVD polycrystalline diamond (730 GPa).

The bulge technique on the other hand is a static experiment which evaluates the mechanical properties of the thin film under biaxial stress conditions. Prior to testing, the thin film is deposited on a suitable substrate. The substrate is then etched away over a circular region, thus producing a region where the film is unsupported. Applying pressure to the film causes it to deflect as a membrane. The radius of curvature of the bulge is monitored using a Michelson's interferometer, where the specimen replaces one of the plain mirrors. The deflection of the centre of the membrane is measured by counting the number of sharp circular fringes produced as a function of pressure. Using this measurement the radius of curvature of the membrane can be determined from which the bulge height is calculated. By accurate measurement of the bulge height as a function of the applied pressure, the stress strain relationship of the film can be obtained. Using this relationship and knowing it's thickness, it is possible to obtain the Young's modulus of the film to a reasonable accuracy (few percent).

Accurate thermal expansion data is especially important when chosing and developing hard materials for use as thin film coatings. Optical and transport properties may be directly affected by thermal expansion of the film and indirectly through stresses both thermal and intrinsic, induced due to the difference in expansion between the film and the substrate. Also the film adherence to the substrate and the resistance of the coating to thermal stress fracture depends strongly on obtaining a good thermal expansion match between the film and substrate. The thermal expansion coefficient of the film is therefore an important parameter when designing windows. The technique for the measurement of the film thermal expansion uses a combination of an optical lever method and electronic detection to continuously observe thermal deformation. The basis of this technique lies in the fact that at room temperature the sample (film + substrate) will be curved due to their different thermal expansion coefficients. A change in temperature causes a change in curvature. It is from this change in curvature that the thermal expansion coefficient of the film can be calculated.

The internal stress is another important film property as its presence within the film not only affects the mechanical properties but also other material properties including the optical properties. Internal stress reduces the adhesion of the film to the substrate which severely limits its usefulness. The techniques chosen to measure stress are the laser scanning technique, the bulge test method and the profilometer method. Both the laser scanning and profilometer techniques are beam curvature methods of measuring stress. That is the stress within the film can be evaluated by measuring the curvature of the substrate on which the film is deposited. The laser scanning technique for stress measurement is the same as that used to measure the thermal expansion, therefore both properties can be measured simultaneously. The same principle applies to the profilometer technique. The deflection of a substrate beam is measured using a surface profilometer. The internal stress can be measured in either of two ways. Firstly

at the free end of the sample clamped at one end, or at the central deflection of the beam clamped at both ends. The length of the scanned segment should be about 10-15mm. This technique was used to measure the room temperature stress present in both MPACVD diamond films and in germanium carbide films. The diamond films were found to be in a state of tensile stress, with values as high as 0.88 GPa for films ranging from 1μm to 13μm thick. The germanium carbide films on the other hand were compressive in nature, with stress values of around 0.025 - 0.04 GPa for films ranging from 14 - 15 μm in thickness. The bulge test technique for measuring stress is the same as that for the measurement of Young's modulus. For compressive films, once the substrate has been etched away over a circular region, the unsupported region will bulge without any pressure applied. If the film is tensile in nature some pressure will be required to bulge the film. The stress is then measured by analysing the bulge height as a function of pressure. For both types of film the deflection of the bulged film is related to the total film stress.

REFERENCES

AWAJI H., SATO S., "Diametral Compressive Testing Method", Journal of Engineering Materials and Technology, Vol. 101, April 1979

BRION D., "Etude Par Spectroscopie de Photoelectrons de la Degradation Superficielle de FeS_2, $CuFeS_2$, ZnS et PbS a l'air at dans l'eau", Applications of Surface Science, Vol. 5, 1980

CARNEIRO F.L.L.E., BARCELLOS A., "Concrete Tensile Strength", Bull. R.I.L.E.M., Vol. 13, 1953

CHARLES R. J., HILLIG W. B., page 511-527 in Symposium on Mechanical Strength of Glass and Ways of Improving it. Florence, Italy, September 25-29, 1961. Union Scientifique continentaie du Verre, Charleroi, Belgium, 1962

DARVELL B.W., "Review: Uniaxial Compression Tests and the Validity of Indirect Tensile Strength", Journal of Materials Science, Vol. 25, 1990

DAVIDGE R.W., "Mechanical Behaviour of Ceramics", Cambridge University Press, 1979

DEOM A.A., BALGEAS D.L., LATURELLE F.G., GARDETTE G.D., FREYDEFONT G.J., "Sensitivity of Rain Erosion Resistance of IR materials to environmental conditions such as temperature and stress", SPIE Vol. 1326, 1990

DRIGGERS G.W., TIDWELL E.D., "Development and Operating Experience on a Zinc-Sulfide window for the Infrared Instrumentation System (IRIS)", SPIE Vol. 1112. "Window and Dome Technologies and Materials", 1989

EVANS A.G.,"A Method for Evaluating the Time-Dependent Failure Characteristics of Brittle Materials - and its Application to Polycrystaline Alumina", Journal of Materials Science, Vol. 7, 1972

EVANS A.G., JOHNSON H., "A Fracture-Mechanics Study of ZnSe for Laser Window Applications", Journal of the American Ceramic Society, Vol. 58 , No. 5-6, May-June 1975

FAIRHURST C., "On the Validity of the 'BRAZILIAN' Test for Brittle Materials", Int. J. Rock Mech. Mining Sci., Vol. 1, 1964

FREIMAN S.W., "Fracture Mechanics of Glass", Glass: Science and Technology, Ed. Uhlmann D.R., Kreidl N.J., Academic Press, 1980

FREIMAN S.W., MECHOLSKY J.J.Jr., RICE R.W., "Influence of Microstructure on Crack Propagation in ZnSe", Journal of the American Ceramic Society, Vol. 58 , No. 9-10, September - October 1975

FREIMAN S.W., WHITE G.S., FULLER E.R.Jr., "Environmentally Enhanced Crack Growth in Soda-Lime Glass", Journal of the American Ceramic Society, Vol. 68 , No. 3, March 1985

FULLER E.R. Jr., "An evaluation of Double-Torsion Testing - Analysis", Fracture mechanics Applied to Brittle Materials, ASTM STP 678, 1979

GRAHAM P.M., PARFITT C., FREELAND C.M., "Development of a Thermal Shock Test Equipment Suitable for Laboratory Use", British Aerospace Report No. HX 7093-0010-TR, 1990

GRENET L., "Mechanical Strength of Glass", Bull. Soc. Enc. Industr. Nat. Paris, (Ser. 5), No. 4, 1899

HAGAN J.T., SWAIN M.V., FIELD J.E., "Stress Corrosion Characteristics of Toughened Glasses and Ceramics", Journal of Materials Science, Vol. 13, 1978

HAN W., TOMOZAWA M., "Mechanism of Mechanical Strength Increase of Soda-Lime Glass by Aging", Journal of the American Ceramic Society, Vol. 72, No.10, October 1989

HAND R.J., "Impact and Fracture Properties of Infra-red and Optical Transmitting Materials", PhD thesis, University of Cambridge, 1987

HAND R.J., FIELD J.E., "Tests on Large Zinc Sulphide Discs and Damaged Zinc Sulphide", BAe report, 1989

HIRAO K., TOMOZAWA M., "Dynamic Fatigue of Treated High-Silica Glass: Explanation by Crack Tip Blunting", Journal of the American Ceramic Society, Vol. 70, No. 6, June 1987a

HIRAO K., TOMOZAWA M., "Kinetics of Crack Tip Blunting of Glasses", Journal of the American Ceramic Society, Vol. 70, No. 1, January 1987b

HOLLAND L., "The Properties of Glass Surfaces", London, 1964

HONDROS G., "The Evaluation of Poisson's Ratio and the Modulus of Materials of a low Tensile Resistance by the 'BRAZILIAN' (Indirect Tensile) Test with Particular Reference to Concrete", Aust. J. Appl. Sci., Vol. 10, 1959

IKEDA K., IGAKI H., TANIGAWA Y., TAGASHIRA K., "Equibiaxial Stress Effect on Fracture Strength of Indented Soda-Lime Glass in Water Environment: An Examination for Dependence on Crack-Tip Blunting", Journal of the American Ceramic Society, Vol. 73, No. 7, July 1990

ITO S., TOMOZAWA M., "Crack Blunting of High-Silica Glass", Journal of the American Ceramic Society, Vol. 65, No. 8, August 1982

KAMAN SCIENCES, "Fracture of ZnS and Si", Private Communication, Kaman Sciences Corp., Colorado Springs, USA

KINGERY W.D., "Factors Affecting Thermal Stress Resistance of Ceramic Materials", Journal of The American Ceramic Society, Vol. 38, No. 1, January 1955

LAWN B.R., FULLER E.R., "Equilibrium penny-like cracks in indentation fracture", Journal of Materials Science, Vol. 10, 1975

LAWN B.R., WILSHAW T.R., "Fracture of Brittle Solids", Cambridge University Press, London, 1975

LEWIS M.H., KARUNARATNE B.S.B., "Determination of High-Temperature K_I - V Data for Si - Al - O - N Ceramics", Fracture Mechanics Methods for Ceramics, Rocks and Concrete, ASTM STP 745, 1981

MATTHEWSON M.J., FIELD J.E., "An Improved Strength-Measurement Technique for Brittle Materials", J. Phys. E., Vol. 13, 1980

MICHALSKE T.A., BUNKER B.C., "Steric Effects in Stress Corrosion Fracture of Glass", Journal of the American Ceramic Society, Vol. 70 , No. 10, October 1987a

MICHALSKE T.A., BUNKER B.C., "The Fracturing of Glass", Scientific American, December 1987b

MICHALSKE T.A., SINGH M., FRECHETTE V.D., "Experimental observation of Crack Velocity and Crack Front Shape Effects in Double-Torsion Fracture Mechanics Tests", Fracture Mechanics Methods for Ceramics, Rocks and Concrete, ASTM STP 745, 1981

OUTWATER J.O., GERRY D.J., "On the Fracture Energy of Glass" *NRL Interim Contract Report*, Contract NONR 3219 (01) (x), AD 640848, University of Vermont, Burlington, Vt., Aug. 1966.

PLETKA B.J., FULLER E.R. Jr., and KOEPKE B.G., "an evaluation of Double-Torsion Testing - Experimental", Fracture mechanics Applied to Brittle Materials, ASTM STP 678, 1979

PRABHU G.M., ULRICHSON D.L., PULSIFER A.H., "Kinetics of the Oxidation of Zinc Sulphide", Ind. Eng. Chem. Fundam., Vol. 23, 1984

QUINN G.D., "Delayed Failure of a Commercial Vitreous Bonded Alumina", Journal of Materials Science, Vol. 22, 1987

RABIE A.M., MEGUID S.A., "An Evaluation of a Probabilistic Engineering Approach to the Failure Prediction of Brittle Materials", Engineering Fracture Mechanics, Vol. 24, No. 2, 1986

RUDNICK A., HUNTER A.R., HOLDEN F.C., "An analysis of the Diametral-Compression Test", Materials Research and Standards, Vol. 3, No. 4, April 1963

SAVAGE J.A., "Infrared Optical Materials and their Antireflection Coatings", Adam Hilger Ltd., 1985

SCHWARTZ R. W., "U.S. Navy Dome Materials Development Program", Third Workshop on Passive Infrared Optical Materials and Coatings, Brussels, March, 1990

SHAW M.C., "Metal Cutting Principles", Clarendon, 1984

SHINKAI N., BRADT R.C., RINDONE G.E., "Fracture Toughness of Fused SiO_2 and Float Glass at Elevated Temperatures", Journal of the American Ceramic Society, Vol. 64 , No. 7, July 1981

SIMMONS C.J., FREIMAN S.W., "Effect of Corrosion Processes on Subcritical Crack Growth in Glass", Journal of the American Ceramic Society, Vol. 64, No. 11, November 1981

SOHN H.Y., DAESOO K., "Intrinsic Kinetics of the Reaction Between Zinc Sulphide and Water", Metall. Trans. B, Vol. 18, No. 2, 1987

TAIT R.B., FRY P.R., GARRETT G.G , "Review and Evaluation of the Double-Torsion Technique for Fracture Toughness and Fatigue Testing of Brittle Materials", Experimental Mechanics, March 1987

TAIT R.B., GARRETT G.G., "A Fracture Mechanics Evaluation of Static and Fatigue Growth in Cement Mortar", Proc. Conf. Fract. Mech. of Conc., Ed. Wittmann F.H., Lausanne, Elsevier, October 1985

TOWNSEND D., FIELD J.E., "Fracture Toughness and Hardness of Zinc Sulphide as a Function of Grain Size", Journal of Materials Science, Vol. 25, 1990

VARDAR O., FINNIE I., "An Analysis of the Brazilian Disk Fracture Test using the Weibull Probabilistic Treatment of Brittle Strength", International Journal of Fracture, Vol. 11, No. 3, June 1975

WAHL J.M., TUSTISON R.W., "Mechanical Enhancement of LWIR Materials via Coatings", SPIE Vol. 1326, "Window and Dome Technologies and Materials II", 1990

WIEDERHORN S.M., "Influence of Water Vapour on Crack Propagation in Soda-Lime Glass", J. Am. Ceram. Soc., Vol. 50, No. 8, 1967

WIEDERHORN S.M., BOLZ L.H., "Stress Corrosion and Static Fatigue of Glass", J. Am. Ceram. Soc., Vol. 53, No. 10, 1970

WIEDERHORN S.M., FULLER E.R.Jr., "Effect of Surface Forces on Subcritical Crack Growth in Glass", Journal of the American Ceramic Society, Vol. 72 , No. 2, February 1989

WIJK G., "Some New Theoretical Aspects of Indirect Measurements of the Tensile Strength of Rocks", Int. J. Rock Mech. Min. Sci. and Geomech. Abstr., Vol. 15, 1978

WILLIAMS D.P., EVANS A.G., "A Simple Method for Studying Slow Crack Growth", Journal of Testing and Evaluation, Vol. 1, No. 4, July 1973

XUE L.A., RAJ R., "Superplastic Deformation of Zinc Sulphide Near its Transformation Temperature (1020°C)", Journal of the American Ceramic Society, Vol. 72 , No. 10, October 1989

APPENDIX

Solid particle impact of CVD diamond films

Z. Feng, Y. Tzeng* and J.E. Field

PCS, Cavendish Laboratory, University of Cambridge, Cambridge, CB3 0HE, UK

* *Plasma Processing Laboratory, 200 Broun Hall, Auburn University, Alabama 36849, USA*

Abstract

Studies of the dynamic impact and static indentation of chemically vapour deposited (CVD) diamond films are described. Polished and unpolished CVD diamond films of ~ 6 to 15 μm thickness, deposited on both silicon nitride and silicon substrates, were investigated. In the dynamic impact experiments, sand particles with impact velocities of 34 m s^{-1} and 59 m s^{-1} were used. Three stages of impact damage were identified; (i) formation of ring cracks, (ii) partial debonding and penetration of the film, and (iii) full debonding and film removal. The first stage is similar to what occurs with natural diamond. However, the last stage, i.e., the material loss mechanism for CVD films, is mainly caused by delamination of the film. Examination of fracture surfaces using scanning electron microscopy (SEM) showed that transgranular fracture of the diamond films was quite common despite the polycrystalline nature of the films. This suggests that the bonding strength between diamond grains is as strong as that within the grains. Finally, static indentation with a tungsten carbide ball of similar size to the sand particles was performed to determine the fracture strength of polished CVD diamond film and to make a comparison with the impact experiments. The fracture tensile strength for CVD diamond films was found to be ~ 2.8 GPa, which is much lower than the reported value of 8.6 to 12 GPa for natural diamonds.

1. Introduction

Since the first report of diamond deposition on non-diamond substrates from the gas phase by Spitsyn and Derjaguin [1] in 1981 and the subsequent confirmation by Matsumoto et al. [2] in 1982 using a modified thermal CVD method, diamond film has attracted a large number of research groups [3] around the world to explore its new synthesis methods, basic mechanisms, and applications. The CVD technology developed in the past ten years has enabled the coating of large area substrates (greater than 30 cm diameter) with thin-film diamond and the production of thick (greater than 1 mm) free-standing diamond plates at rates exceeding 1mm per hour. It has thus made it possible for many diamond properties [4] to be utilized in new and innovative applications [5]. One of the most promising applications is the use of CVD diamond films as coating materials either for protecting various kinds of substrates, including optical windows, against chemical and mechanical attack, or for providing low-wear and low-friction surfaces. For these applications, the mechanical properties of the diamond coatings are crucial. Whether the CVD diamond is as strong as natural diamond remains an open question. More needs to be known about the role of the defects in the diamond grains and the bonding between grains. The present work describes studies of the response of the coatings to low velocity (less than 60 m s^{-1}) impact [6] and to static indentation, from which the mechanical strength of diamond coatings can be measured.

2. Experimental

2.1 Diamond film specimens

Four CVD diamond films were used: (a) polished film (with a surface roughness of 8 nm CLA and a film thickness of ~ 15 μm), deposited on a silicon nitride substrate by microwave plasma CVD; (b) unpolished film (with a surface roughness of 1 μm CLA and a film thickness of ~ 6 μm), deposited on silicon by hot filament CVD with (100) facets dominating; (c) unpolished film. The preparation method, surface roughness, thickness and

2

substrate were the same as (b), but diamond grains with (111) facets dominating; and (d) unpolished free standing film deposited by hot filament CVD with a grain size of 2-4 μm and a film thickness of 25 μm. Films (a), (b) and (c) were used in the solid impact experiments and film (d) for fractographic study following bending. Film (a) was also used in static indentation experiments to determine fracture strength and to make a comparison with results obtained from impact experiments. Figure 1 shows optical and SEM micrographs of the CVD diamond films used in the present work. Detailed information about the preparations and characterization: of the CVD diamond films can be found in references [7,8].

2.2   Solid particle impact experiments

A schematic diagram of the solid particle impact apparatus is shown in Figure 2a. It uses a fast gas stream to accelerate the particles along a steel tube. The particles are fed into the steel tube from a sand reservoir using compressed air and the flux is controlled by means of a turn-table in the reservoir. The impact velocity of the particles was measured using a cross-correlation method to an accuracy of 4%. The specimen was mounted on a holder which was placed near the exit of the steel tube and a thin rubber sheet with a hole of ~ 4 mm diameter was used to define the impact area. The solid particles used were natural sieved sand grits with dimensions of 300 to 600 μm and of a block-type shape (Figure 2b). The mean particle mass was 190 μg.

The experiments involved first exposing a specimen to the impact of sand particles for a certain time, then examining the damage by using optical microscopy and SEM. Normal impact (impact direction 90° to the specimen surface) was chosen because this causes maximum damage with brittle materials. The flux rate was 4.6 kg m^{-2} s^{-1}. Two impact velocities, i.e., 34 m s^{-1} and 59 m s^{-1}, were chosen for the experiments. All experime were performed at ambient conditions with a temperature of ~23°C and a relative humidity of 50%.

2.3   Static indentation experiments

Static indentation was performed to determine the fracture strength of the polished CVD diamond film and to make a comparison with the results obtained from the impact experiments. They were performed using an Instron 1122 machine, operated at a loading speed of 0.05 mm min^{-1}. A tungsten carbide ball with a Young's modulus of ~650 GPa, a hardness of ~18 GPa and of 0.39 mm diameter was used as the indenter. An optical microscope, viewing the indented surface from an angle of ~ 30°, was used to monitor the presence of a ring crack after the indenter was lifted. A Nomarski interference optical microscope was also used to photograph the ring crack and loaded area. The fracture strength was obtained from Hertz theory (Appendix I) by using the measured critical load and ring crack size.

3.   Results and Discussion

3.1   Sand particle impact of polished CVD diamond films

In these experiments impact velocity and exposure time were varied and the conditions for film cracking and delamination obtained. The first experiment was performed at an impact velocity of 59 m s^{-1}, with a flux rate of 4.5 kg m^{-2} s^{-1} and an exposure time of 10s and ring cracks were found on the surfaces after impact. The experiment was then carried out at a lower sand velocity, i.e., 34 m s^{-1}, with the same flux rate and for the same time of exposure, and again ring cracks were formed on the surfaces but with a lower crack density (see Figure 3a and 3b). There was no significant difference in the sizes of ring cracks observed at these two velocities. No diamond film removal occured at this stage for both impact velocities.

Experiments were then performed at an impact velocity of 59 m s^{-1} for an increased time of impact. It was found that film removal from the substrate started after an exposure time of ~70s. Figure 4a shows an SEM micrograph of the area where the film has delaminated. Figure 4b is an optical micrographs from the edges of the impacted area. The edge shape

4

shown in Figure 4b appears to follow the boundaries defined by ring cracks. However, this feature was not found everywhere.

The film surface adjacent to a delaminated area can be used to study what happens just before film removal starts because of the lower impact flux in this area due to the shadowing effect the rubber mask. Examination by optical microscopy showed that the film surface became increasingly wavy (which is particularly clear when the surface is looked at from a glancing angle) compared with other areas. This is presumably due to partial debonding of the film from the substrate. The fractured edge tends to curve out of the substrate surface because of residual stresses in the film. An examination of the same surface area with SEM (Figure 4c) also shows that penetration of the film has also taken place at this stage of impact damage.

The damage process for a CVD diamond film by sand particle impact follows the sequence: (i) formation of ring cracks, (ii) debonding and/or penetration of the film, and (iii) removal or delamination of the film from the substrate. The formation of ring cracks at the initial stage is a typical fracture phenomenon for brittle materials. This was also observed in the impact of natural diamond by sand particles using the same apparatus [9]. However, the material removal mechanisms are very different; in the case of CVD diamond, the premature removal of the film is caused by the delamination; while in the case of natural diamonds it occurs only when ring or cone cracks intersect to separate small volumes of diamond from the bulk.

3.2   The fracture mechanisms

The fracture mechanism of CVD diamond was then studied by examining fracture surfaces caused by sand impact using SEM. Figure 5a shows a fracture surface on a polished CVD diamond film where a half ring crack occurs near the film edge. The fracture surface is so smooth that it is difficult to see any individual diamond grains. Because CVD diamond films are usually polycrystalline it is desirable to know whether grain boundaries are weak points or not. In order to clarify this question, experiments were carried out using unpolished

5

CVD diamond films, in which grains and grain boundaries could easily be identified. In these experiments, the impact velocity was 34 m s⁻¹.

Figure 5b shows a fractured edge on a (100) facet dominated diamond film. The arrowed region clearly indicates a transgranular fracture across a crystal. Figure 5c shows a similar micrograph for a (111) facet dominated film, where a single crystal was clearly cut through by a crack. These results show that transgranular fracture is common with CVD diamond films impacted by sand particles. However, it is not clear whether the transgranular fracture initiated inside a grain or from a grain boundary

Since the fracture surfaces described above were produced by dynamic loading. It is of interest to determine whether transgranular fracture can also take place under static loading conditions. Fracture surfaces produced by bending a piece of free-standing film were examined. Figure 6 shows SEM micrographs obtained at the same area with different view angles. They again show transgranular fracture.

Transgranular fracture of CVD diamond films has also been reported by Hoff et al. [10], Mecholsky et al. [11]. This phenomenon appears to be quite common with CVD diamond films and suggests that either strong bonding between diamond grains exists in them or the diamond grains are much weaker than single crystal natural diamond because of their high defect density. Fallon and Brown [12] found that the grain boundaries of CVD diamond films are composed mainly of diamond rather than other forms of carbon. This result also suggests that the bonding between diamond grains can be as strong as that within the grains.

3.3   Fracture strength of CVD diamond film

The fracture strength of the film can be estimated by measuring the contact area and calculating the impact force during erosion using Hertz theory, assuming that the contact between the sand particles (treated as sphere) and the CVD diamond film (treated as a half space) is elastic and quasi-static (for details see Appendix II). The effects of film thickness and adhesion between film and substrate are temporarily ignored in this calculation and will be

discussed later. The results are given in Table 1, together with results from erosion experiments on natural diamond. In the calculation (see also Figure 8) the following elastic constants for the sand particles and natural diamond were used: E_0=65.7 GPa, ν_0=0.25, R=150-300 µm (two values are given for each radius), ρ=2650 kg m^{-3}, E=1140 GPa, ν =0.07.

Table 1 shows that the measured sizes of ring crack are generally in good agreement with the values estimated, considering that the sizes of sand particles range from 300 to 600 µm and that the sand particles are not spheres as assumed (Figure 2b). The observed ring cracks are similar to those found in the erosion of natural diamond [9]. However, the critical load, or impact velocity, for producing ring cracks in these two kinds of diamonds for the same time of impact (10s) by sand particles are very different. For the same particle size, for example, R=150 µm, the critical load of CVD diamond film is smaller than 14 N, while for natural diamond it is ~ 62 N. It appears that the CVD diamond film is weaker than bulk natural diamond. This can also be seen in the critical contact pressures of < 5 GPa and ~ 8 GPa for CVD diamond film and bulk natural diamond, respectively. These strength data can only be regarded as rough estimates because of the uncertainties in the determination of the critical load, the particle size and shape, and the effects of the substrate. In order to measure the fracture strength of the CVD diamond film more accurately, static indentation experiments were conducted.

3.4   Fracture strength measured by static indentation

In this technique the load and the indenter geometry can be controlled. Moreover, critical load and ring crack size can be measured. Therefore, meaningful comparisons between experimental results and calculated values can be made. The results are given in Table 2. Figure 7 shows a typical ring crack produced by indentation. In Table 2 the measured ring crack diameter is larger than the calculated values. Assuming a half space of diamond film, the measured value is ~30% larger than the calculated diameter, while in the case of assuming a half space of silicon nitride it is ~ 6% larger. This is a reasonable agreement, considering that

7

(i) the actual Young's modulus of CVD diamond films are usually lower than that of natural single crystal diamond [13-15], resulting in a larger contact area, and (ii) it is well-known that the measured diameters of the ring cracks are usually between 10 to 30 % larger than the calculated elastic contact diameter [16-19].

In a theoretical analysis of the elastic contact size in a coating system, El-Sherbiney and Halling [20] found that for a coating system consisted of a hard coating with a Young's modulus about three times the substrate and a coating thickness of $t/a_0 \sim 0.5$ (where t is the coating thickness and a_0 is the contact radius calculated by Hertz theory), the actual contact size on the coating surface is almost the same as that given by the Hertz equation assuming a half space of the coating material. This is the case for the present work. A similar result was also found in the theoretical analysis of the stress field for hard coating systems by van der Zwaag and Field [21]. This analysis explains why the measured values were in good agreement with the calculated values in spite of the assumption that the interfacial strength between diamond film and the substrate is perfect. Wu et al.[22] found that the interfacial strength of thin (~ 0.1 μm) diamond-like carbon films on a silicon substrate has a great effect on the strength of the film measured in an indentation fatigue experiment. The small influence of interfacial strength on the size of ring cracks, and the strength measurements for the CVD diamond film in the present study is probably due to having a relatively thicker film ($t/a > 0.5$). However, the interfacial strength still plays an important role in the material removal process as shown in the present work.

Table 2 gives a critical contact pressure (load divided by crack area) of 3.2 GPa for the formation of a ring crack by static indentation. Compared with the contact pressures given in Table 1 it appears that the diamond film was overloaded in the impact experiments. The critical contact pressure under static indentation corresponds to a radial tensile stress of ~ 2.8 GPa for the diamond film. This is comparable to the fracture strength (~ 1 to 5 GPa) measured by Windishmann [14] for CVD diamond films using a Bulge test technique. Using an indentation technique, Howes [23] measured the fracture strength of natural diamonds with 0.5 mm tungsten carbide balls, and reported values from 10.5 to 13.5 GPa for the contact pressures

giving radial tensile stresses in the range of 8.6 to 12 GPa depending on the particular crystallographic face that was indented. These values are much higher than that of CVD diamond films. This is presumably due to the high density of defects and the presence of residual stresses in the CVD diamond films.

4. Conclusions

CVD diamond films were studied by means of sand particle impact as well as static indentation experiments. The following conclusions can be drawn from this study:

(a) The impact damage of CVD diamond films proceeds with (i) formation of ring cracks, (ii) debonding and penetration of the film, and (iii) removal of the film due to delamination from substrate.

(b) For the CVD diamond films used (with a thickness of ~15 μm and a thickness to contact radius ration of ~ 0.5), Hertz theory allows the fracture strength to be estimated reasonably accurate.

(c) The tensile strength of CVD diamond film is ~ 2.8 GPa. It is lower than that of a natural diamond, which is ~ 8.6 and 12 GPa obtained under similar conditions.

(d) Transgranular fracture of the film is very common, suggesting that bonding between diamond grains is as strong as that of the diamond grains themselves.

References

1   B. V. Spitsyn, L.L. Bouilov and B.V. Derjaguin, *J. Crystal Growth*, *52* (1981) 219.

2   S. Matsumoto, Y. Sato, M. Kamo and N., Setaka, *Japn. J. Appl. Phys*, *21* (1982) L183.

3   R. Messier, J. T. Glass, J.E. Butler, and R. Roy, Proc. of the 2nd Int. Conf. on New Diamond Sci. and Tech., Washington D.C., Mat. Res.Soc., Pittsburgh, Pa., (1991).

4   J.E. Field, 'The properties of diamond' edited by J.E. Field, Academic Press: London, (1979).

5   Y. Tzeng, M. Yoshikawa, M. Murakawa and A. Feldman (editors), Applications of Diamond Films and Related Materials, Elsevier, 1991.

6   J.E. Field and J.P. Dear (editors), 'Proc. of 7th Int. Conf. on Erosion by Liquid and Solid Impact', Cavendish Laboratory, Cambridge, England, Sept. 1987.

7   T. Srivinyunon, R. Philips, C. Cutshaw, A.J. Joseph and Y. Tzeng, Proc. of 2nd Int. Conf. on New Diamond Sci. and Tech., Mat. Res.Soc., Pittsburgh, Pa., (1991) 581-586.

8   K. Nishimura, *Diamond Optics IV, SPIE*, in press (1991).

9   Z. Feng and J.E. Field, *J. Hard Material, 1* (1991) 273-287.

10   H.A. Hoff, A.A. Morrish, K.A. Snail, J.E. Butler, and B.B. Rath, 'New Diamond Sci. and Tech., Mat. Res.Soc., Pittsburgh, Pa, (1991) 773-778.

11   J.J. Mecholsky, Y. L. Tsai and W.R. Drawl, to be published in *J. Appl. Phys.* (1991).

12   P. Fallon and L.M. Brown, *Diamond Conference Abstract*, Oxford (1991). Unpublished.

13   B.S. Berry, W.C. Pritchet, J.J. Cuomo, C.R. Guarnieri and S.J. Whitehair, *Appl. Phys. Lett., 57* (1990) 302.

14   G.F. Cardinale and R.W. Tustison, *SPIE Proc. 1325* (1990).

15   H. Windischmann, G.F. Epps and G.P. Ceasar, 'New Diamond Sci. and Tech., Mat. Res.Soc., Pittsburgh, Pa , (1991) 767-772.

16   K.L. Johnson, J.J. O'Connor and A.C. Woodward, *Proc. R. Soc. Lond. A 334* (1973) 95-117.

17   R. Warren, *Acta Metall, 26* (1978) 1759-1769.

18   R. Mouginot and D. Maugis, *J. Matt. Sci., 20* (1985) 4354-4376.

19   M.M. Chaudhri and E.H. Yoffe, *Phil. Mag. A, 44* (1981) 667-675.

20   M.G.D. El-Sherbiney and J.Halling,*Wear, 40* (1976) 325 .

21   S. van der Zwaag and J.E. Field, *Phil. Mag. A, 46* (1982) 133-150 .

22   T.W. Wu, A.L. Shull and R. Berriche, *Surf. Coating and Tech., 47* (1991) 696-709

23   V.R. Howes, *Proc. Phys. Soc., 80* (1962) 78.

24 H. Hertz, Collected Works, Leipzig Barth, 1 (1882) 174

25 S.P. Timoshenko and J.N. Goodier, 'Theory of Elasticity', 3rd edn, MaGraw-Hill, New York, (1970) 420.

Appendix I

Hertz theory of elastic contact [24]

For a sphere of radius R in contact with a half space under a load, F, the radius of the circle of contact, a, and the maximum tensile stress at the contact circle, σ_m, are given by:

$$a^3 = \frac{4}{3} \frac{FRk}{E} \,, \tag{1}$$

$$\sigma_m = \frac{1-2\upsilon}{2\pi a^2} F = \frac{1}{2}(1-2\upsilon) P_m \,, \tag{2}$$

where $k = \frac{9}{16}[(1-\upsilon^2 + (1-\upsilon_0^2)\frac{E}{E_0}]$, and E, υ and E_0, υ_0 are the Young's moduli and Poisson ratios of the half-space and the indenter respectively. P_m is the mean pressure between the indenter and the flat specimen.

Appendix II

Theory of single particle impact [25]

For a sphere of radius R impacting with a half space at a velocity of V (Figure 8). Hertzian contact theory can be applied, provided that the contact circle expands at a rate less than the velocity of elastic waves and quasi-static analysis conditions are satisfied.

The maximum load F_m is given by,

$$F_m = (\frac{5\pi\rho}{3})^{3/5} (\frac{4k}{3E})^{-2/5} R^2 V^{6/5} \,. \tag{3}$$

12

The mean pressure is

$$P_m = \frac{1}{\pi}(\frac{5\pi\rho}{3})^{1/5} (\frac{4k}{3E})^{-4/5} V^{2/5} .$$ (4)

The maximum contact radius is,

$$a_m = \sqrt{\frac{F_m}{\pi P_m}} ,$$ (5)

where ρ is the density of the impacting sphere and other parameters are as previously defined.

Figure captions

Figure 1

CVD diamond specimens. (a) polished film on a silicon nitride substrate with a thickness of ~15 μm, (b) unpolished film on a silicon substrate with a thickness of ~ 6 μm and showing (100) crystal facets, (c) unpolished film on silicon substrate with a thickness of ~ 6 μm and showing (111) crystal facets , (d) unpolished free standing film with a thickness of ~ 25 μm.

Figure 2

Erosion apparatus (a) and sand particles (b).

Figure 3

Optical micrographs of eroded CVD diamond film surfaces obtained at an impact velocity of ~ 34 m s^{-1} for 10s. (a) near the edge and (b) at the central area.

Figure 4

Optical and SEM micrographs of CVD diamond film surfaces obtained after impact at a velocity of ~59 m s^{-1} for 70s. (a) exposure area where film has been delaminated, (b) an area near the broken edge, (c) an SEM micrograph in the same area as (b).

Figure 5

SEM micrographs of fractured surfaces produced by sand particle impact. (a) on the polished film, (b) on the unpolished (100) facet dominated film, (c) on the unpolished (111) facet dominated film.

Figure 6

SEM micrographs of fractured surfaces produced by bending a free standing film to fracture.

Figure 7

A typical optical micrograph of the ring crack produced by indenting a tungsten carbide ball on the polished microwave plasma CVD diamond film deposited on silicon nitride.

Figure 8

A schematic diagram of Hertz contact for calculating the contact size and load in the static indentation and impact experiments. E_0, υ_0 and E, υ are the Young's moduli and Poisson ratios of the sphere and the half space, a is the radius of contact and r the radius of ring/cone crack.

Table 1. Results of erosion experiments

Material	Impact velocity / m s^{-1}	Measured diameter of ring crack / μm[a]	Calculated diameter of contact area / μm[c]	Calculated impact load / N	Calculated contact pressure / GPa
CVD dia. film	34 (10s)	38 - 96	54 - 108	14 - 57	5.0
Nat. dia. bulk	34 (1000s)	42[b]	54 - 108	14 - 57	5.0
Nat. dia. bulk	140 (10s)	150[b]	95 - 189	62 - 247	8.8

a. Measured from optical micrographs.
b. Averaged value.
c. Calculated from Hertz theory using particle diameters of 150 to 300 μm.

Table 2. Results of static indentation experiments

Tungsten carbide ball / mm	Critical load for ring crack / N	Measured diameter of ring crack / μm	Calculated diameter of contact / μm	Critical contact pressure / GPa	Tensile strength / GPa
0.39	7.9	56	43[a] / 53[b]	3.2	2.8
0.5[c]	/	/	/	10 -13.5[c]	8 - 12

a. Assuming diamond film as half space. b. Assuming silicon nitride as half space, using E_0=310 GPa (hot pressed), υ_0=0.26. c. Obtained from reference [4] for natural diamond.
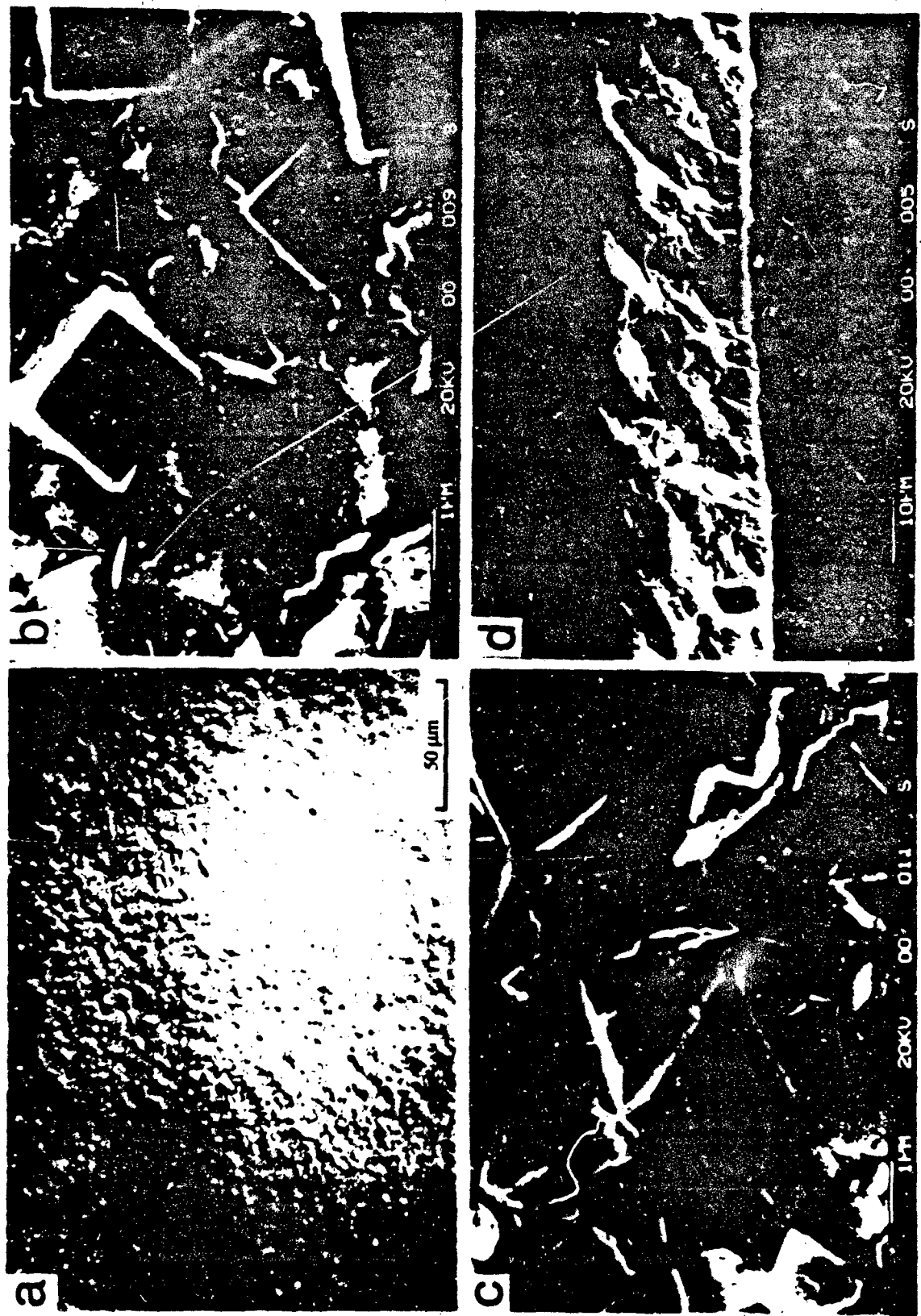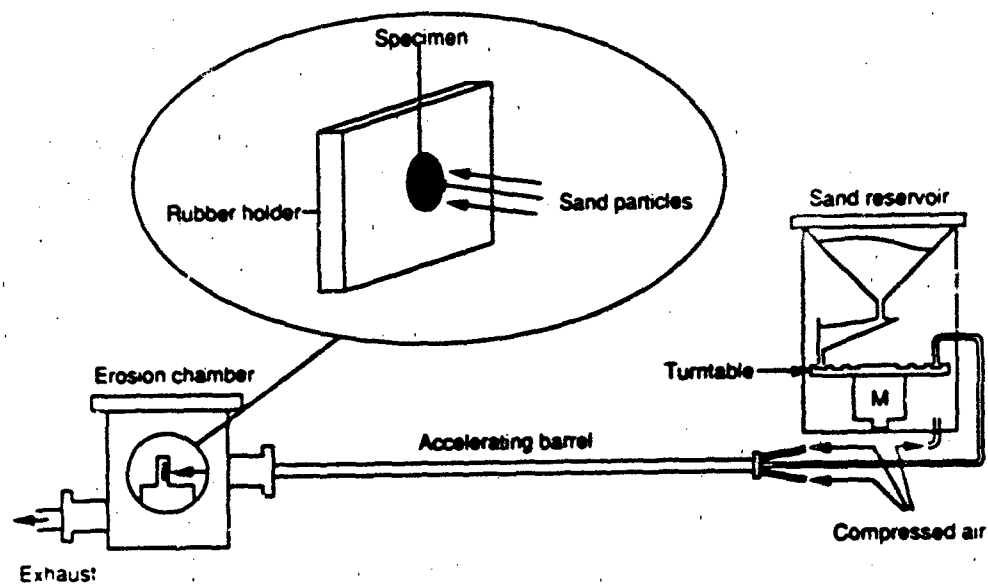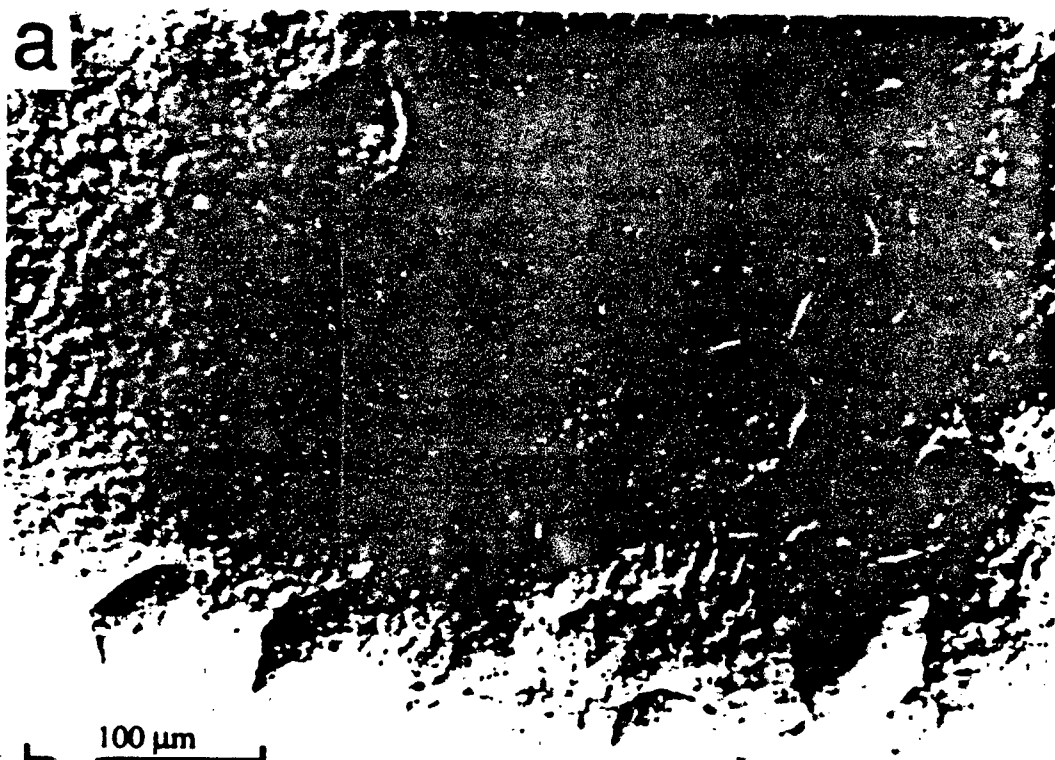
Figure 1

a

Specimen

Rubber holder — Sand particles

Sand reservoir

Erosion chamber

Turntable

M

Accelerating barrel

Compressed air

Exhaust

b

1mm   20KV   S

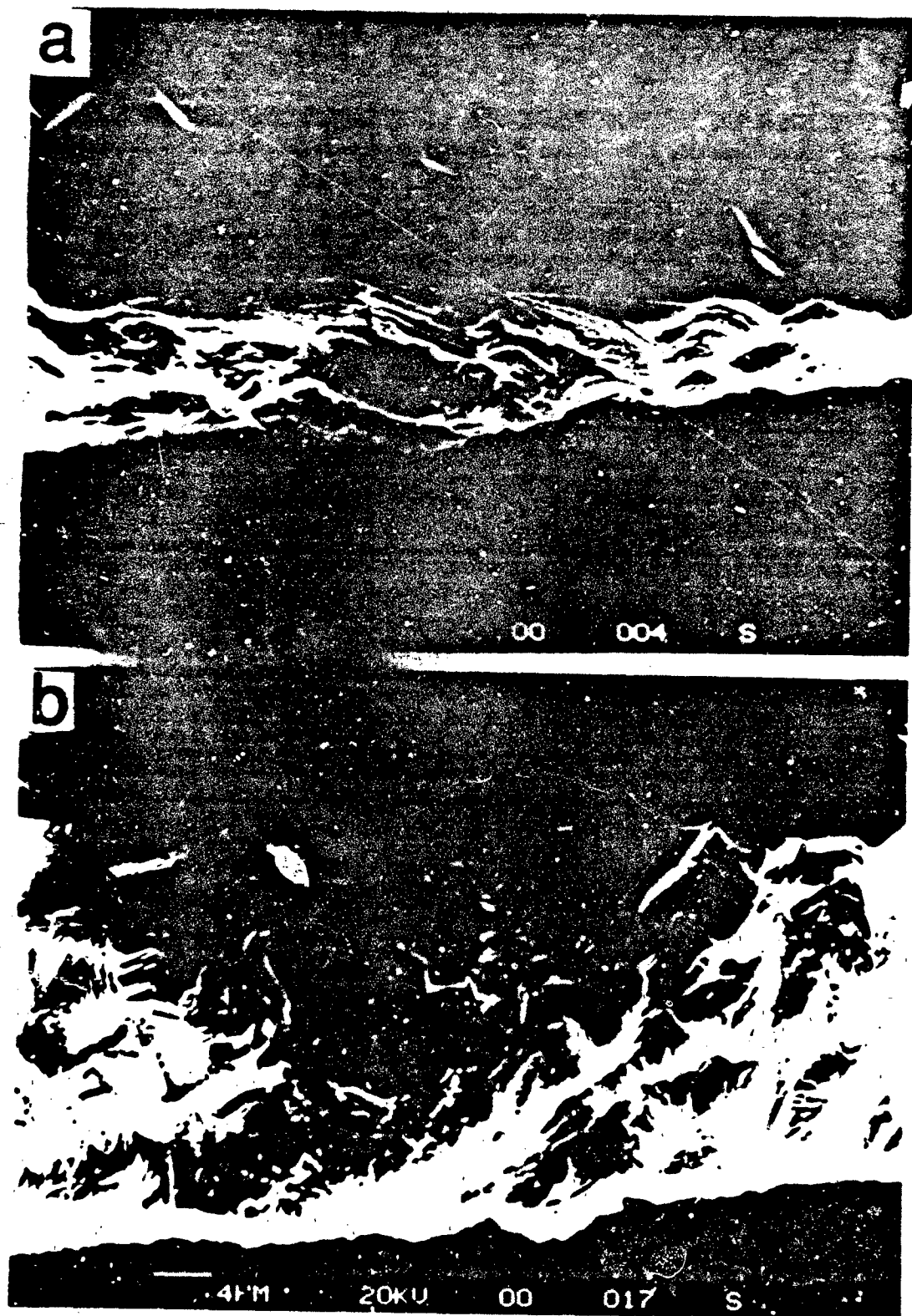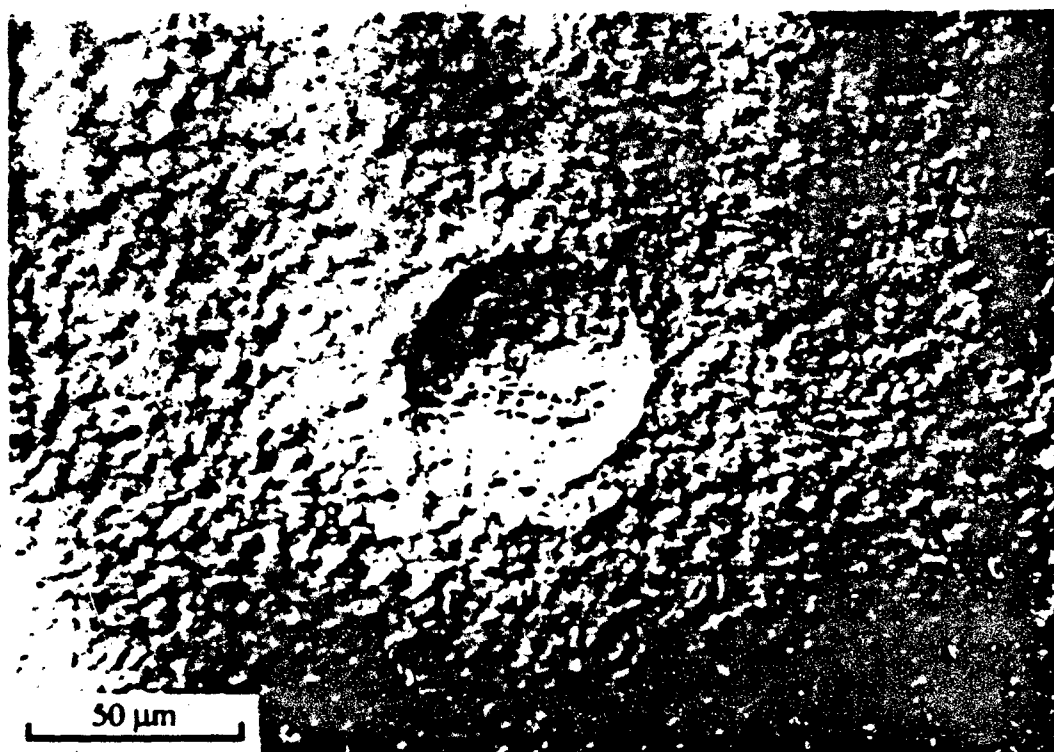Figure 2

a

100 μm

b

1(X) μm

Figure 3

100 µm

Figure 4

Figure 5

Figure 6

Figure 7
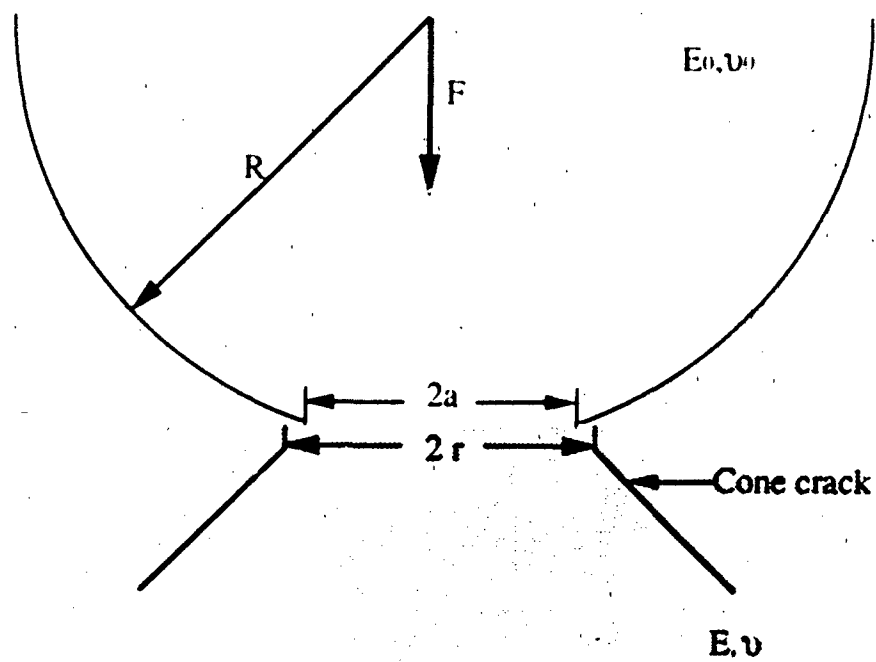
Figure 8

END

FILMED

DATE: 2-92

DTIC